

Temperature Map of the Virgo Cluster of Galaxies Observed with ASCA

R. Shibata ¹, K. Matsushita ², N. Y. Yamasaki ³, T. Ohashi ³,
M. Ishida ¹, K. Kikuchi ⁴, H. Böhringer ², and H. Matsumoto ⁵

shibata@astro.isas.ac.jp

ABSTRACT

The temperature distribution of the intracluster medium (ICM) in the Virgo cluster of galaxies has been derived from extensive mapping observations with ASCA covering an area of 19 deg². In the spectral analysis, the inner region within a radius of $\sim 60'$ from M87 is characterized by an ICM temperature of $kT \sim 2.5$ keV with little variation. On the other hand, the outer regions indicate significant variation of the temperature with an amplitude of about 1 keV. The temperature map was produced from the hardness ratio (H.R.) values with a resolution of about $5'$. Besides the previously reported hot region with $kT > 4$ keV between M87 and M49, several hot regions with $kT = 3 - 4$ keV are detected in the cluster outskirts. The auto-correlation function for the H.R. variation shows that the temperature variation is correlated within a size of about 300 kpc, suggesting that gas blobs falling in the Virgo cluster have a typical size of groups of galaxies. A correlation with the velocity dispersion of member galaxies shows that only the north-west region indicates an unusually large β_{spec} value of 2 – 4. The upper limit for extended non-thermal emission in the Virgo cluster is obtained to be $L_X \sim 9 \times 10^{41}$ ergs s⁻¹ in the 2 – 10 keV band. We discuss that these features consistently indicate that the Virgo cluster is in a relatively early stage of the cluster evolution.

Subject headings: galaxies: clusters: individual (Virgo) — intergalactic medium — X-rays: galaxies

¹Institute of Space and Astronautical Science, 3-1-1, Yoshinodai, Sagami-hara, Kanagawa 229-8510 Japan

²Max-Planck-Institut für extraterrestrische Physik, Giessenbachstrasse Postfach 1603, Garching, D-85740, Germany

³Department of Physics, Tokyo Metropolitan University, 1-1 Minami-Osawa, Hachioji, Tokyo 192-0397 Japan

⁴Space Utilization Research Program, National Space Development Agency of Japan, 2-1-1 Sengen, Tsukuba, Ibaraki 305-8505, Japan

⁵Center for Space Research, Massachusetts Institute of Technology, 77 Massachusetts Avenue, Cambridge, MA 02139-4307, USA

1. Introduction

Clusters of galaxies are believed to be evolving over cosmological time scales. Studies of the redshift evolution of the X-ray luminosity function of clusters have been carried out, and the observed results indicate that the most luminous clusters tend to be sparse in the redshift range greater than about 0.3 (Rosati et al. 1998). Recently, evidence for the evolution of individual clusters have been obtained in the form of temperature variations in the intracluster medium (ICM) from more than 10 systems (Henrikson & Markevitch 1996; Henry & Briel 1996; Honda, et al. 1996; Davis & White 1998; Donnelly et al. 1998; Markevitch et al. 1998; Churazov et al. 1999; Markevitch et al. 1999; Molendi et al. 1999; Shibata et al. 1999; Watanabe et al. 1999). It is considered that gas heating is caused by collisions between subclusters and main clusters, and the temperatures are raised by several keV. Detailed mappings of the temperature distribution in nearby clusters would give us information about the size and number distribution of the colliding blobs, which can be used to constrain theoretical models of structure formation.

The Virgo cluster of galaxies is the nearest cluster, with the enormously large angular extent of about 6° in radius. It is classified as Bautz-Morgan type III (Bautz & Morgan 1970), and Rood-Sastry type F (Rood & Sastry 1971) and shows a highly irregular morphology (Abell, Corwin, & Olowin 1989). This feature suggests that the cluster is undergoing dynamical evolution.

In the optical band, a catalogue containing 2096 galaxies within an area of $\sim 140 \text{ deg}^2$ roughly centered at $\alpha \sim 12^{\text{h}}15^{\text{m}}$ and $\delta \sim 13^\circ$ was produced by Binggeli, Sandage, & Tammann (1985) and Binggeli & Cameron (1993). Optical properties of about 1300 member galaxies, such as morphologies, number counts, and heliocentric velocities, have been examined. The distance to the cluster was measured with various methods and derived to be 12 – 22 Mpc with a large uncertainty (summarized in Jacoby et al. 1990). Recently, Federspiel, Tammann, & Sandage (1998) derived 20.7 ± 2.4 Mpc based on the 21 cm line width-absolute magnitude relation in the B band. Fukugita, Okamura, & Yasuda (1993) and Yasuda, Fukugita, & Okamura (1997), based on the Tully-Fisher relation for spiral galaxies, showed evidence that the galaxy distribution is largely elongated in the line of sight from 12 to 30 Mpc. Jacoby et al. (1990) showed that the M49 and M86 subclusters were located $\sim 0.6 \pm 0.7$ Mpc and 1.2 ± 0.6 Mpc farther than the M87 subcluster on average. The M86 distance is consistent with the result by Neilsen & Tsvetanov (2000, 2.5 ± 1.5 Mpc).

In the X-ray band, the first indication of very extended emission over angular scales of 10° was obtained with non-imaging detectors on board the Ginga satellite (Takano 1990; Koyama, Takano, & Tawara 1991). The X-ray emission is strongly peaked at M87, and well described by a β model with $\beta = 0.436$, $R_c = 1'.62$, as previously obtained by the Einstein IPC data within $100'$ from M87 (Fabricant & Gorenstein 1983). In the southern outer part (2° away from M87), the X-ray surface brightness distribution shows significant flattening with $\beta \sim 0.357$. The ICM temperature around M87 was almost constant with $kT \sim 2$ keV, but the Ginga data suggested a temperature rise toward M49.

The ROSAT all-sky survey covered the Virgo cluster region between November 1990 and

January 1991 in the energy range 0.1 – 2.4 keV (Böhringer et al. 1994). On large scales, the X-ray morphology generally traces the galaxy distribution (Schindler, Binggeli, & Böhringer 1999). However, the M49 halo is much smaller in the X-ray image compared to the optical appearance of the galaxies around M49. The X-ray surface brightness around M87 can be fitted by the β model with $\beta = 0.45$ and $R_c = 2'.3$. Although the overall temperature distribution around M87 is consistent with the Ginga result within $\sim 1^\circ$, ROSAT showed no evidence for the temperature rise around M49. Recently, mapping observations from ASCA have detected an unusual hot region between M87 and M49 with a temperature twice as high as the surrounding value of 2 keV (Kikuchi et al. 2000). This provides clear evidence that the Virgo cluster is undergoing strong dynamical evolution.

In this paper, we have significantly expanded the mapped area and present a nearly complete view of the brightness and temperature distributions of the ICM. The closeness of this cluster enables us to look into detailed structures in the temperature distribution at a resolution of a few hundred kpc for the first time. Results on the metal distribution will be reported in a separate paper (Shibata et al. 2000). We assume the distance to be 20 Mpc (e.g., Federspiel, Tammann, & Sandage 1998), and a $1'$ angular separation corresponds to 5.8 kpc. The solar number abundance of Fe relative to H is taken as 4.68×10^{-5} (Anders & Grevesse 1989) throughout this paper.

2. Observation and Analysis

2.1. ASCA Observations

The ASCA observations of the Virgo cluster have been carried out in 3 occasions: December 1996 and June 1997 with a combined exposure of 200 ksec (northwest region of M87, Matsumoto et al. 2000), June 1998 for 280 ksec (linking region between M87 and M49, Kikuchi et al. 2000), and June 1999 for 210 ksec (region around M87), respectively. There are other 19 pointings on known X-ray sources whose locations are within the Virgo system. Including these data, the total number of pointings is 60 and the covered sky area is $\sim 19 \text{ deg}^2$, respectively. Figure 1 shows the regions so far observed with ASCA. The radius of each circle is $22'$ corresponding to the field of view (FOV) of the Gas Imaging Spectrometer (GIS; Ohashi et al. 1996; Makishima et al. 1996). The observation log is shown in table 1.

The ASCA satellite (Tanaka, Inoue, & Holt 1994) carries four identical grazing-incidence X-Ray Telescopes (XRT, Serlemitsos et al. 1995; Tsusaka et al. 1995). The point spread function (PSF) of the XRT has a cusp-shape peak with the half power diameter of $3'$. Two Solid-state Imaging Spectrometers (SIS0 and SIS1, Burke et al. 1991) and two GISs (GIS2 and GIS3) are placed at the focal planes of the four XRTs. Because of the 3 times larger FOV of the GIS than the SIS, this paper deals with the GIS data only. The GIS covers an energy range from 0.7 to 10 keV, with a spectral resolution of 8% FWHM at 6 keV.

All the GIS data were obtained in the normal pulse-height (PH) mode. We screened the data with a telescope elevation angle from the Earth rim $> 5^\circ$, and with an attitude aberration from the average $< 1'$. Flare-like events due to background fluctuations (Ishisaki 1996) and data when the spacecraft was in high background regions, such as the south Atlantic anomaly (SAA), were also excluded. The cosmic X-ray background (CXB) was estimated from the archival blank-sky data which was taken during 1993 – 1994 for a total exposure time ~ 560 ksec after data screening. Although the diffuse soft X-ray emission from the North Polar Spur (NPS), which is the most prominent part of Loop I (Egger & Aschenbach 1995), is located in the south-east direction of the Virgo cluster (Snowden et al. 1995), it was confirmed that its influence on the background spectrum was negligible in the ASCA energy band (see section 3.1). The long-term variability of the non X-ray background (NXB) of the GIS (Ishisaki 1996) was corrected for. In the spectral analysis, the data from GIS2 and GIS3 were summed into a single spectrum.

Figure 2 shows the GIS image in the low ($0.5 \sim 2.0$ keV) and the high ($2.0 \sim 10.0$ keV) energy bands. These images are smoothed by a Gaussian function with $\sigma = 1.5'$, but no corrections are made for the background, the vignetting and the point spread function (PSF) of the XRT. The X-ray image of almost the whole cluster in the energy band above 2 keV has been obtained here for the first time. The image shows a generally similar structure to the low band one, but some hard sources are clearly seen (e.g. NGC4388 and VPC0866). The X-ray brightness distribution is strongly peaked at M87 in both energy bands. This feature is similar to the luminosity-weighted distribution of member galaxies, but a simple number-density distribution of galaxies shows a peak closer to M86 (Binggeli, Sandage, & Tammann 1985; Binggeli, Tammann, & Sandage 1987; Schindler, Binggeli, & Böhringer 1999). The X-ray emission is clearly extended over more than 2° around M87, and several discrete sources, both background objects and bright member galaxies, are easily recognized. In the typical outer region at 2.3° northwest of M87 (i.e., positions 2002N, 2003N and 2004W), the intensity of the cluster emission is 0.6–0.7 times that of the total background level (the sum of the non X-ray and the cosmic X-ray background). The linking region between M87 and M49 shows significant X-ray emission in both energy bands, confirming that the 2 subclusters are connected with ICM.

2.2. Elimination of Discrete Sources

Several discrete sources are clearly seen in Figure 2. These sources have to be removed from the data before we look into the ICM properties. We prepared a source mask, which masks out the contribution from contaminating sources, for the spectral analysis. The 3 bright galaxies showing extended emission, M87, M86, and M49, are treated separately by fitting the data with two temperature models.

The source-detection algorithm adjusted for the ASCA mapping data has been developed for the CXB study by Ueda et al. (1999), and applied to the Virgo data by Kikuchi et al. (2000) who detected 231 source candidates. However, the strong intensity gradient around M87 and the

systematic contamination due to the stray light of the XRT make direct application of this method to the present data difficult. The latest mapping data obtained in June 1999 (see table 1) and the additional pointing data near M87 are particularly difficult to analyze with this method. On the other hand, the flux level around M87 within $\sim 1.5^\circ$ is about an order of magnitude higher than that in the south region. Therefore, the remaining contamination in this region would be relatively small, even if the discrete-source subtraction is incomplete. Because of this, we prepared the source mask by picking up recognizable sources with the following method for each pointed field.

As a first step, we produced GIS images in three energy bands: $0.5 \sim 2.0$ keV, $2.0 \sim 10.0$ keV and $0.5 \sim 10.0$ keV, for all 60 pointings. Next, in each image we searched manually for X-ray peaks and extended excess emission. For each detected source, the size of the source mask is determined by the source intensity. We require the source mask to satisfy the condition that the remaining flux of the source outside the mask should be less than $1/3$ of the surrounding ICM level. As a result, we produced 50 source masks which could exclude source candidates with X-ray fluxes $> 5 \times 10^{-13}$ ergs $\text{cm}^{-2} \text{s}^{-1}$ in the $2 - 10$ keV band. All the bright sources listed in the bright source catalogue of the ROSAT all-sky survey (Voges et al. 1999; Schwöpe et al. 2000) were excluded with this mask.

The number of sources detected in this work is much smaller compared with the source candidates reported by Kikuchi et al. (2000), who picked up the sources with a $2 - 10$ keV flux $> 1 \times 10^{-13}$ ergs $\text{cm}^{-2} \text{s}^{-1}$. To evaluate the goodness of the present source removal, we estimated the expected fraction of the flux contamination. As for the GIS, the detection limit with a pointing of ~ 20 ksec, which is the typical exposure time in the present mapping observation, is estimated to be $\sim 2 \times 10^{-13}$ ergs $\text{cm}^{-2} \text{s}^{-1}$ in $2 - 10$ keV band (Ueda et al. 1999). Therefore, we may assume that all the unsubtracted sources have this flux level in the worst case. The $\log N - \log S$ relation obtained with the ASCA (Ueda et al. 1999) predicts that the expected number of sources at this flux level is $\sim 2.5 \text{ FOV}^{-1}$. Therefore, the maximum remaining flux per FOV after the source-mask application becomes $\sim 5 \times 10^{-13}$ erg $\text{cm}^{-2} \text{s}^{-1}$. Though the detection limit increases in the region near M87 where the ICM brightness is much higher, the expected remaining flux per FOV decreases since the expected number of sources is small at the high flux level. The contaminating fraction, which is the ratio of the remaining flux to the ICM intensity in the GIS FOV, is less than 5% in the region within 3° from M87 and $\sim 10\%$ in the outer regions. This flux level is comparable to the field to field fluctuation of the CXB. The net effect is the reduction of the best-fit ICM temperatures within the statistical errors, assuming that the remaining sources have a power-law spectrum with a photon index of 1.7.

To confirm that the resultant ICM temperatures are not significantly affected by the unsubtracted weak sources, we compared the present temperature values with the previous results by Kikuchi et al. (2000; northwest and south regions of M87). The temperature values are mostly consistent within the statistical error, and there is no systematic feature such as the correlation with the ICM intensity or with the distance from M87. We conclude that the present source-detection procedure causes no systematic problems, even in the faint flux regions.

2.3. Stray Light Contamination

Some fraction of the photons from outside of the FOV reaches the focal plane due to the XRT properties. These photons are called *stray light* and complicate the data analysis for largely extended sources. It comes from the surrounding sky region within the angular radius of 2° from the center of the FOV. The correct estimation of the stray light is particularly important in the analysis of spatially resolved spectral features in the ICM. We evaluate the amount of the stray light by utilizing the ray-tracing simulation (Tsusaka et al. 1995) and include its effect in the XRT response function used in the spectral analysis. For this estimation, we first need to know the precise surface brightness distribution of the cluster. However, the highly irregular morphology of the Virgo cluster cannot be approximated by simple analytic models such as the β model. The ROSAT all-sky survey (RASS; Böhringer et al. 1994) data give a complete image with significantly better angular resolution than the ASCA. Therefore, these data are used here as the template for the surface brightness profile. We select the PSPC data only above 0.5 keV, which gives better matching with the ASCA band. A spatially uniform background, obtained from a blank sky region, is subtracted from the Virgo RASS data.

To justify the use of the RASS image, we have to check that the observed GIS image is well reproduced in the energy range below 2 keV by the ray-tracing simulation. For the incident spectrum, we assume a MEKAL model (Mewe, Lemen, & Oord 1986) with constant spectral parameters over the cluster area with a temperature of 2.0 keV and a metal abundance of 0.3 solar, respectively. These values have been previously derived for the Virgo cluster (see e.g., Koyama, Takano, & Tawara 1991; Matsumoto et al. 2000). The actual data indicate spatial variation in temperature as shown later, and the ray-tracing code has a systematic error of about 10%. Allowing for these errors, we found that the RASS image reproduced the soft-band GIS image with the satisfactory accuracy. The relative deviation of the simulated image from the observed one is less than 10% in all regions. We then estimated the stray light effect based on this template image.

The XRT response calculation based on the RASS image is performed over a radius of 2° for each pointed field (coordinates are listed in table 1). This size covers the range in which the stray light causes significant effects. The XRT response function is computed with the assumption that the cluster gas is isothermal. This approximation, which enables us to perform spectral fits for individual regions, is useful for the first-order estimation of the spectral parameters (Honda et al. 1996). The ray-tracing simulation also allows us to trace back the origin of detected photons. We noticed that the regions $1^\circ \sim 1.2^\circ$ from M87 were strongly affected by the emission from the cluster center, and the central flux within $r = 10'$ contributed about 20% of the detected flux. Excluding the regions within about 1° from M87, M86 and M49, almost half of the detected photons are always occupied by the flux from the pointed sky region in the field of view.

3. Results

3.1. Temperature Distribution

Pulse-height spectra are produced by accumulating the GIS data in each pointed field. Most of the regions are tested with single temperature thermal models (MEKAL) in the energy band 0.8 – 10.0 keV. The interstellar absorption is fixed at the Galactic value [$N_{\text{H}} = (1.6 - 2.7) \times 10^{20} \text{ cm}^{-2}$, Stark et al. 1992]. The plasma temperature, normalization, and metal abundance are the free parameters. For three bright galaxies, M87, M86 and M49, we include an additional soft X-ray component to model the galaxy emission ($kT \sim 1 \text{ keV}$; Matsumoto et al. 1996; Awaki et al. 1994; Matsushita et al. 1994). The fitted model consists of the 2 components: the hot component (ICM) described by a MEKAL model, and the cool component described either by the MEKAL or by the MEKAL + Bremsstrahlung model in which the temperature of the bremsstrahlung is fixed to 10 keV. The 10 keV Bremsstrahlung is known to give an empirical approximation to the spectra for low-mass X-ray binaries (Makishima et al. 1989, Matsushita et al. 1994, Matsumoto et al. 1997). The two-dimensional distribution of the ICM temperature derived from the individual spectral fits is shown in the top-left panel of figure 3. The top-right and the bottom panels show projected temperature distribution along the north-south and the east-west directions, respectively. The errors indicate 90% statistical limits. The best-fit temperatures are summarized in table 1.

As shown in figure 3, the temperature is about 2.5 keV around M87 and decreases slightly to $\sim 2.0 \text{ keV}$ with a large fluctuation in the northern region of M87. In the southern region, the average temperature at 2° from M87 is still $\sim 2.5 \text{ keV}$. In the linking region between M87 and M49, we confirm the unusually high temperature recently reported by Kikuchi et al. (2000). The temperature in the M49 region is $\sim 2.2 \text{ keV}$ and drops to $\sim 1.5 \text{ keV}$ with radius.

The X-ray surface brightness is evaluated for 3 different regions. The region around M87 with a radius of $0.4^\circ - 2.5^\circ$ (covered area $\sim 12.2 \text{ deg}^2$) indicates a 2.0 – 10.0 keV brightness of $(1.05_{-0.07}^{+0.07}) \times 10^{-14} \text{ ergs cm}^{-2} \text{ s}^{-1} \text{ arcmin}^{-2}$, the M49 region with a radius of $0.4^\circ - 1.0^\circ$ (covered area $\sim 2.5 \text{ deg}^2$) shows $(1.52_{-1.39}^{+2.05}) \times 10^{-15} \text{ ergs cm}^{-2} \text{ s}^{-1} \text{ arcmin}^{-2}$, and the region between M87 and M49 with the declination of $+9^\circ 00' \sim +11^\circ 00'$ (covered area $\sim 2.8 \text{ deg}^2$) indicates $(6.33_{-2.38}^{+1.79}) \times 10^{-15} \text{ ergs cm}^{-2} \text{ s}^{-1} \text{ arcmin}^{-2}$, respectively.

Examples of the spectra are shown in the top panel of figure 4 for the hot (pos-1508E and 1509E, $\sim 110'$ away from M87) and the cool (pos-1513N and 2001N, $\sim 120'$ away from M87) regions. The data are well represented by a single MEKAL model. The bottom panel shows the ratios of the observed data and the XRT responses, i.e., the effective areas of XRT, used in the spectral fit. Since the responses are very similar with almost no energy dependence in the energy range above $\sim 2 \text{ keV}$, the temperature difference between the two regions is evident. The best-fit temperatures are obtained to be $2.65_{-0.16}^{+0.15} \text{ keV}$ and $1.71_{-0.09}^{+0.11} \text{ keV}$ for the hot and cool regions, respectively. The possible origins for the systematic error of the temperature are the error in the estimated contaminating spectrum from M87, the remaining contribution from the masked-out sources, and

the fluctuation of the CXB and NXB. The integrated systematic error on the temperature is estimated to be less than 0.2 keV, which is much less than the temperature difference between the 2 regions.

Within 10' from M87, a significant variation in the metal abundance has been reported by Matsumoto et al. (1996). Therefore, the spectrum in pos-0001, within $\sim 25'$ from M87, cannot be fitted with a simple two temperature model ($\chi^2_\nu = 1.71$). Spectral analysis around the bright M87 region will be presented in a separate paper (Shibata et al. 2000).

There is a flux contamination from the NPS around M49. The PSPC spectrum was reported by Irwin & Sarazin (1996) to be $kT = 0.15$ keV and the 0.5–2.0 keV flux was 0.6×10^{-15} ergs cm $^{-2}$ s $^{-1}$ arcmin $^{-2}$, respectively. This is only $\sim 4\%$ of the ICM level in the 0.8–2.0 keV band (used for the spectral analysis) and $\sim 10\%$ in the 0.7–2.0 keV band (for the hardness ratio analysis in section 3.2), respectively. Compared with the single temperature fit, the best-fit ICM temperatures change by about +0.2 keV which is within the statistical error in this region. Considering also that the affected regions are confined around M49, we may say that the effect of the NPS is not significant for the present temperature results.

Figure 5 shows the frequency distribution of the ICM temperature based on the spectral fits for the GIS FOV unit. Shaded and unshaded portions correspond to the data within 2.5° centered on M87 and for all the data in the Virgo field, respectively. We fitted the distribution with a Gaussian function and obtained an average temperature of $\bar{T} = 2.33$ keV with $\sigma_{\bar{T}} = 0.28$ keV within 2.5° from M87 and $\bar{T} = 2.28$ keV with $\sigma_{\bar{T}} = 0.43$ keV for all regions, respectively. The assumption of a constant temperature gives a χ^2 value of 351 with 37 degrees of freedom within 2.5° from M87. Therefore, there is a significant temperature variation over angular scales larger the GIS FOV ($\sim 44'$ or ~ 260 kpc).

3.2. Spatial Variation of the Hardness Ratio

In this section, we estimate the small-scale ($\sim 5'$) variation of the ICM temperature based on the hardness ratio analysis.

Hardness ratios (H.R.) are calculated from the background-subtracted counting rates in the energy bands 2.0–7.0 keV and 0.7–2.0 keV. This energy division is chosen to maximize the temperature sensitivity for the spectra with $kT \sim 2$ keV. The top panel of figure 6 shows the H.R. for each pointed field ($r \sim 22'$) as a function of the distance from M87 with filled circles. There is a small gradient from M87 to M49 and the remarkable hard region between M87 and M49. There is a sharp minimum at $\sim 85'$ from M87, which is caused by the reflection property of the XRT. This angle corresponds to the boundary where the single reflection light from the secondary mirror disappears so that the spectrum becomes softer in larger angles. The apparent H.R. values are thus strongly dependent on the XRT response and the surface brightness distribution. Therefore we need to correct for these effects before converting them to the temperature.

The conversion from the H.R. values to temperatures is performed based again on the ray-tracing simulation. Open circles in the top panel of figure 6 show simulated H.R. values for an isothermal ICM with $kT = 2.0$ keV. The assumed spectral model is MEKAL with a metal abundance of 0.3 solar, and the RASS image is used for the surface brightness profile. Since the plasma temperature is a simple and smooth function of the H.R., the ratio of the observed to simulated H.R. indicates the correct temperature in each position (i.e., $kT = 2.0$ keV when the data to model ratio is unity). The effect of the variation of the metal abundance is such that the temperature changes by ± 0.3 keV for an abundance change of ± 0.2 solar, respectively. Since the temperature change is within the statistical error, the abundance variation does not significantly affect the temperature results. The middle panel in figure 6 shows the corrected H.R. ($= \text{H.R.}_{\text{obs.}} / \text{H.R.}_{\text{sim.}}$, hereafter C.H.R.) values which now corresponds to the temperature as indicated in the right axis. As a result, the minimum at $\sim 85'$ has disappeared. In order to check the adequacy of the above H.R. temperatures, we again performed the ray-tracing simulation assuming the obtained distribution of the H.R. temperatures, and compared the resultant simulated H.R. values with the observed ones, as shown in the bottom panel. The dispersion of the C.H.R. has become considerably smaller than in the isothermal case (middle panel), which confirms that the the temperature calculation has been consistently performed.

For the 53 pointed fields represented by the single temperature model, the correlation between the temperatures derived from the C.H.R. and from the spectral fit is plotted in Figure 7. Except for two pointed fields (pos-5002S and 5003S, open square) which indicate very low metal abundance (< 0.1 solar) and low temperature (< 1.3 keV) compared with the model spectrum for the simulation, the temperature values agree well. If we fit the correlation with a linear function, a slope of 0.99 ± 0.01 is obtained with a χ^2_ν value of 0.72 (d.o.f. = 51). Based on this agreement, we look into the small-scale temperature variation using the C.H.R.

The two-dimensional map of the temperature is calculated from the C.H.R. and shown in Figure 8. The C.H.R. is calculated for a $20' \times 20'$ square region, and the center of its integrated region is shifted by a $5'$ step in order to raise the photon statistics. Therefore, the temperature map essentially indicates running means for the temperature variation. The XRT response and the vignetting effect are taken into account. The source mask mentioned in section 2.2 is also applied. Since three bright galaxies M87, M86 and M49 contain a cool spectral component, these regions indicate lower H.R. values. The one-dimensional variation of the C.H.R. is shown in figure 9 along the 5 paths indicated in the right panel. This plot also shows the errors in temperature. The 5 paths shown here are as follows; (A) connects the positions of M87 and M49, (B) runs through the high temperature region in the linking region of M87 and M49, (C) is the west-east cut passing through M87, (D) includes the high temperature region at 1.7° north-west of M87, and (E) connects M87 and M86, respectively.

Figure 8 and 9 show that the region within about $60'$ from M87 has little variation of the ICM temperature, except for the inner region ($r \sim 15'$) in which the cool ISM component exists. On the other hand, the outer region shows a significant variation of temperature. As already seen in the

H.R. feature in figure 3, we can recognize that the periphery of M87 is hotter than the M49 region, and the linking region between both galaxies shows a significantly harder emission.

3.3. Spatial Scale of Temperature Variation

As shown in figure 8 and 9, we have detected significant temperature variation in the ICM. The data enable us a quantitative evaluation of the spatial scale for the temperature variation. We will investigate it by calculating the auto-correlation function (ACF). The cell size is $10' \times 10'$, and the temperature is calculated from the C.H.R. as described in the previous section. The ACF is calculated for the two dimensional distribution of the C.H.R., as a function of the angular distance θ between two cells. This is given by the following formula:

$$W(\theta) = \left\langle \frac{\{S(\mathbf{r}_i) - \bar{S}\} \{S(\mathbf{r}_j) - \bar{S}\}}{\bar{S}^2} \right\rangle_{\theta_{ij}=\theta} \quad (i \leq j, \quad i = 1, 2, \dots, N)$$

$$(\theta_{ij} = |\mathbf{r}_i - \mathbf{r}_j|)$$

where $S(\mathbf{r}_i)$ is the C.H.R. at the i -th position, \bar{S} is the average ratio ($= 1.20$ corresponding to 2.43 keV), N is the total cell number, and $\langle \rangle$ denotes an angular average, respectively. If we assume that the hardness ratio is a random variable obeying a Gaussian distribution with a mean of \bar{S} and variance of σ_S^2 , the standard deviation of the ACF is given by

$$\sigma_{W(\theta)} = \frac{1}{\sqrt{N}} \left(\frac{\sigma_S}{\bar{S}} \right)^2 .$$

In this calculation, we exclude the regions showing the two temperature components: near M87, M86 and M49. The resultant ACF is plotted in figure 10 (filled circle). A significant correlation exists within an angular distance of $\sim 1.5^\circ$. On larger angular scales, the correlation strength drops to almost zero and shows no features.

There could be a systematic effect due to the large-scale temperature gradient centered on M87, as recognized in figure 3. This gradient can be represented by a power-law function as $T(r) = 3.83 \times r^{-0.12}$ [keV] for a radius range $30' \sim 150'$. The expected ACF profile with this gradient is shown with the broken line in figure 10. The feature due to the temperature gradient is too small to account for the ACF profile presently obtained for the Virgo cluster, in particular on angular scales of $\sim 1^\circ$ (~ 350 kpc).

The obtained auto-correlation feature can be interpreted in the following way. The strong correlation in $\theta < 1^\circ$ suggests that up to this scale the ICM tends to have the same temperature. This angular scale corresponds to an actual size of 300 kpc at the Virgo cluster. On larger angular scales, the temperature distribution seems to be random within the statistical error. We note that significant temperature fluctuations with a scale of individual GIS fields ($\sim 44'$ or ~ 260 kpc) as seen in figure 5 is consistent with the auto-correlation result.

3.4. Correlation with Galaxy Properties

The ICM temperatures are compared here with the properties of galaxies available in the VCC (Binggeli, Sandage, & Tammann 1985, Binggeli & Cameron 1993), which gives us number counts, average heliocentric velocities, and velocity dispersions (σ_r) of the local member galaxies. We adopt the ICM temperature evaluated in each pointed field (shown in section 3.1). The galaxy properties are mean values in a radius of 1.5° centered on the GIS-FOV, thus averaging is here over a larger field than for the temperature, which is necessary to obtain enough statistics.

Galaxy counts and average velocities both indicate a weak positive correlation with the ICM temperature. We recognize that cooler regions tend to show a lower galaxy count and a lower velocity than other regions. No significant correlation is seen for the luminosity-weighted galaxy count, however.

The left panel of figure 11 shows a correlation between the temperature and the velocity dispersion in the whole cluster. The symbols indicate different regions. Triangles are for the northwest of M87 (around M86), filled circles are within 2.5° from M87 except for the northwest region, and open circles are the remaining regions, respectively. The clustering of the same symbols suggests that galaxies form distinct groups. In particular, the group around the velocity dispersion of $\sim 800 \text{ km s}^{-1}$ is clearly different from others.

The presence of a distinct group is also suggested by the $\beta_{\text{spec}} (= \mu m_p \sigma_r^2 / kT)$ value drawn in the left panel of figure 11. This is the ratio between the velocity dispersion of galaxies and the thermal energy of the ICM. The general cluster region indicates a typical value of $\beta_{\text{spec}} \sim 1.0 \pm 0.5$, and the northwest region shows unusually large β_{spec} values above 2.0. If galaxies and gas are in dynamical equilibrium, we expect β_{spec} to be about unity. The map of β_{spec} values in the right panel of figure 11 shows that these high β_{spec} values are distributed around M86 and in the northern direction. This indicates that the ICM has not reached dynamical equilibrium, which is probably related to a subcluster merger in the M86 region.

3.5. Inspection of the Extended Non-thermal Emission

Recently, the advanced sensitivity of BeppoSAX for extended hard X-ray emission above 10 keV has enabled the detection of non-thermal emission from several clusters (Coma cluster; Fusco-Femiano et al. 1999, A2199; Kaastra et al. 1999, A2256; Fusco-Femiano et al. 2000). Since the Virgo cluster has a relatively low ICM temperature ($\sim 2.5 \text{ keV}$), the thermal emission rapidly decreases above 6 keV, as shown in the bottom panel of figure 12. This allows us to search for extended non-thermal emission with the ASCA GIS in the energy band below 10 keV.

Spectral data were summed up, and the overall spectrum of the ICM was produced by excluding several exceptional regions. The pointing on M87 (pos-0001, $r < 22'$) shows extremely strong emission characterized by two temperature component spectra and has been removed from the

average spectrum. The hot region between M87 and M49 and the region around M86 and M49 show significant deviation from the average temperature of about 2.5 keV, and have been excluded. As a result, the average Virgo spectrum is produced for a radius of $0.4^\circ - 2.5^\circ$ from M87 with a covered area of $\sim 12.2 \text{ deg}^2$. This includes 36 pointing data with a temperature of $2.2 \pm 0.5 \text{ keV}$ after the source mask was applied as mentioned in section 2.2.

The combined spectrum was first fitted with the MEKAL model in the energy range 0.8–10.0 keV. Concerning the very high statistics, systematic errors need to be included in the fit. The current response of the GIS requires a systematic error of 0.5% to obtain an acceptable fit for the spectral data of the Crab nebula. Therefore, we include the same systematic error in fitting the overall Virgo spectrum. The plasma temperature, normalization, and metal abundances of Fe, S and Si are free parameters. The interstellar absorption is fixed at the average Galactic value in this direction ($N_H = 2.55 \times 10^{20} \text{ cm}^{-2}$). A single temperature model gives a best-fit χ_ν^2 value of 1.23 (d.o.f. = 322), and a two-temperature model yields $\chi_\nu^2 = 1.10$ (d.o.f. = 320). The two-temperature model is acceptable at the 90% confidence limit. The best-fit temperatures are $3.67_{-0.52}^{+0.53} \text{ keV}$ and $1.38_{-0.13}^{+0.09} \text{ keV}$, respectively, and the metal abundances are $Z_{\text{Fe}} = 0.16_{-0.03}^{+0.04}$ solar, $Z_{\text{S}} = 0.52_{-0.09}^{+0.10}$ solar, and $Z_{\text{Si}} = 0.33_{-0.06}^{+0.08}$ solar, respectively. This two-temperature model should be regarded as a simple empirical representation of the ICM component to put constraints on the non-thermal component. In other words, it is the most simple model which can represent multi-temperature components shown in figure 3 and 8 within the photon statistics. Therefore, only the Fe abundance which strongly depends on the intensity of L- α emission line is somewhat uncertain. The parameter values are summarized in table 2, and the fitted spectrum is also shown in the top panel of figure 12. The X-ray flux in the integrated region, already mentioned in section 3.1, is $(1.09_{-0.14}^{+0.23}) \times 10^{-14} \text{ ergs cm}^{-2} \text{ s}^{-1} \text{ arcmin}^{-2}$ in the 2.0 – 10.0 keV band.

Next, we include in the fit a power-law component to examine the possibility of non-thermal emission. The model consists of the two-temperature MEKAL and the power-law (PL) components. Since a fit with a free power-law index Γ could not constrain the parameter, we assume it to be 1.7. The fitting results are summarized in table 2. The χ^2 value shows no improvement by the addition of the PL component. The upper limit of the PL flux is $9.52 \times 10^{-16} \text{ ergs cm}^{-2} \text{ s}^{-1} \text{ arcmin}^{-2}$ in the 2.0 – 10.0 keV band, which corresponds to less than 9% of the total flux. Figure 12 shows the spectral components (thermal component and the upper limit of the PL component) together with the CXB and the NXB spectra. The BGD components become dominant above 6 keV. We evaluate the influence of the background uncertainty to the upper limit of the PL component. Since the uncertainty in the background spectra are estimated to be $\sim 10\%$ (CXB) and 6% (NXB) for the single GIS FOV, the uncertainty for the combined Virgo spectrum (~ 31 GIS FOV) is estimated to be 1.8% for CXB and 1.1% for NXB, respectively. If we take the lowest possible NXB flux, the upper limit on the PL component becomes 14% larger than the previous result ($1.09 \times 10^{-15} \text{ ergs cm}^{-2} \text{ s}^{-1} \text{ arcmin}^{-2}$).

In figure 12, we recognize that the upper limit of the PL component is lower than the CXB level by a factor of ~ 8 . The upper limit for the PL flux and luminosity for the whole integrated

region are 4.78×10^{-11} ergs cm^{-2} s^{-1} and 2.28×10^{42} ergs s^{-1} in 2 – 10 keV, respectively. If we attribute this flux to contaminating sources fainter than the detection limit ($\sim 2 \times 10^{-13}$ ergs cm^{-2} s^{-1}), the number of the sources should be about 240. However, the $\log N - \log S$ relation (Ueda et al. 1999) indicates that only 30% of the PL flux can be due to unresolved contaminating sources. On the other hand, the integrated flux from low mass X-ray binaries (LMXB) in the member galaxies can contribute to the hard X-ray spectrum. The optical Luminosity (L_B) in the integrated region ($0.4^\circ - 2^\circ.5$ from M87 excluding M86) is estimated to be $1.07 \times 10^{12} L_\odot$ from the VCC data (Binggeli, Sandage, & Tammann 1985). Because the discrete-source flux is proportional to the stellar content given by the relation of $L_X^{\text{LMXB}} / L_B \sim 10^{-3.81}$ (Matsushita, 2000), the total flux from LMXBs is 6.38×10^{41} ergs s^{-1} , which corresponds to about 28% of the upper-limit PL flux.

By subtracting these known contributions, the remaining PL component can have a luminosity of 9.12×10^{41} ergs s^{-1} in the 2 – 10 keV band. This is the upper limit for the diffuse emission in the Virgo cluster. Compared with the recently reported hard X-ray emission from some clusters (e.g., Coma cluster; Fusco-Femiano et al. 1999, A2199; Kaastra et al. 1999, A2256; Fusco-Femiano et al. 2000), the present upper limit for the Virgo cluster is substantially lower by 1 – 2 orders of magnitude.

4. Discussion

4.1. Temperature Variation and Heating Mechanism of ICM

Significant temperature variation has been observed in the Virgo cluster, as shown in section 3.1 and 3.2. It is characterized by a systematic increase of the fluctuation range at larger radii (figure 3). The amplitude of the temperature variation when the data are integrated in the GIS FOV (a diameter of $\sim 44'$ or ~ 260 kpc) is > 2 keV, which is significantly larger than the statistical fluctuation (figure 5). The temperature variations in finer scales are also examined based on the H.R. as shown in figure 8 and 9. In figure 10 the typical scale of the H.R. is estimated to be $< 1^\circ$ based on the auto-correlation analysis. These features indicate that the variation occurs with a crude spatial scale of ~ 300 kpc. In addition to the irregular morphology in the optical and X-ray band, the temperature distribution has shown a new aspect of the Virgo cluster in that the ICM is undergoing a strong dynamical evolution.

Let us look into the heating and cooling mechanisms of the ICM based on the temperature structure. We assume that the heating is caused by an infall of gas into the gravitational potential or by subcluster mergers. It is believed that the formation and evolution of rich clusters takes several 10^9 yr which is a significant fraction of the Hubble time. The time scales relevant for the gas heating are relaxation times for collisions for proton-proton (p-p), proton-electron (p-e) and electron-electron (e-e), respectively, in which the p-e collision takes the longest relaxation time (see Sarazin 1988). This is given by, $t_{\text{eq}(p,e)} \approx 1 \times 10^8 \text{ yr } (T_{\text{gas}}/2.5 \text{ keV})^{3/2} (n/1 \times 10^{-3} \text{ cm}^{-3})^{-1}$,

where T_{gas} is the average ICM temperature (\sim electron temperature) and n is the typical ICM number density around M87. Therefore, the ICM temperature is raised in $\sim 10^8$ yr after the initial heating. The cooling time is given by, $t_{\text{cool}} \approx 5 \times 10^{10} \text{ yr } (n/1 \times 10^{-3} \text{ cm}^{-3})^{-1} (T_{\text{gas}}/2.5 \text{ keV})^{1/2}$, indicating that the cooling is negligible except for the central region of the cluster. Therefore, X-ray temperature (electron temperature) is a good indicator for the local plasma temperature.

The X-ray surface brightness mainly indicates the plasma density, since the variation of emissivity is a slow function of the temperature at $kT \sim 2 \text{ keV}$. The time scale for a local density fluctuation to be smoothed out is determined by the sound crossing time,

$$t_{\text{sound}} \approx 4 \times 10^8 \left(\frac{T_{\text{gas}}}{2.5 \text{ keV}} \right)^{-\frac{1}{2}} \left(\frac{D}{300 \text{ kpc}} \right) \text{ yr},$$

where D is the linear distance of the temperature variation. This indicates that a gas density (or surface brightness) structure disappears in much faster than 1×10^9 yr. The temperature variation, on the other hand, would be smoothed out with the time scale of thermal conduction. This is given by,

$$t_{\text{cond}} \approx 2 \times 10^9 \left(\frac{n}{1 \times 10^{-3} \text{ cm}^{-3}} \right) \left(\frac{T}{2.5 \text{ keV}} \right)^{-\frac{5}{2}} \left(\frac{\ln \Lambda}{40} \right) \left(\frac{D}{300 \text{ kpc}} \right)^2 \text{ yr},$$

where $\ln \Lambda$ is the Coulomb logarithm which is nearly independent of density or temperature for $T_e > 4 \times 10^5 \text{ K}$. This is much longer than the sound crossing time, and it is reasonable that temperature variation persists even though no structure is seen in X-ray morphology.

The observed image of the Virgo cluster is very smooth. Böhringer et al. (1994) could fit the ROSAT radial profile with a single β model with an exception only in the southern region. Since the volume emissivity is proportional to $n^2 \sqrt{T}$, the plasma density should be very smooth in the whole cluster. This means that in most of the region the density disturbance should have occurred more than 4×10^8 yr ago. On the other hand, the presence of the high and low temperature regions indicate that these regions have been heated up less than about 2×10^9 yr ago. This time scale is rather short compared with the Hubble time, and we may conclude that the Virgo cluster is still evolving with local gas heating occurring in the cluster outskirts which have low ICM density.

The estimated distance scale for the temperature variation ($\sim 300 \text{ kpc}$) is larger than the size of typical galaxies, and close to that of galaxy groups. It seems reasonable to suppose that the gas and galaxies have formed certain clumps of this size before falling into the gravitational potential of the main cluster. Numerical simulations of the bottom-up structure formation predict just the same features (Frenk et al. 1996). The high temperature regions probably trace the heating front where small groups have recently encountered and merged with the ICM in the main cluster.

The Virgo cluster provides us with the best close-up view of ICM features on 100 kpc scales. It would be difficult to resolve such features in more distant clusters because of the angular resolution and limited statistics available with ASCA. However, ASCA and ROSAT observations have detected spatial temperature structures from many clusters over several hundred kpc to 1 Mpc

scales. Significant asymmetric temperature structures are observed from the following systems: A115 (Shibata et al. 1999), A754 (Henrikson & Markevitch 1996), A1367 (Donnelly et al. 1998), Coma cluster (Honda, et al. 1996, Watanabe et al. 1999), Centaurus cluster (Churazov et al. 1999), A2142 (Henry & Briel 1996), A2255 (Davis & White 1998), A2319 (Molendi et al. 1999), Cygnus A cluster, A3667, A2065 (Markevitch et al. 1999), A85 and A2657 (Markevitch et al. 1998). Note that these results mostly correspond to large-scale mergers in clusters. Therefore, small-scale (a few hundred kpc) temperature variations such as seen in the Virgo cluster may well be missed in the past observations. It is likely that such small temperature structures would exist in many clusters, in particular in the outer regions where the conduction time scale is long. These features, if observed in future, would provides us with important knowledge about the evolution process of clusters.

4.2. M86 and M49 Subclusters

The β_{spec} distribution shown in figure 11 indicates that the ICM and member galaxies have not reached dynamical equilibrium in some regions. In the previous section, we discussed that the gas heatings could have occurred through infalls of group-size blobs. Here, we examine X-ray and optical properties of 2 known subclusters in the Virgo system, M86 and M49, in some detail.

M86 is located in the northwest of M87 with an angular separation of $\sim 80'$ (~ 0.3 Mpc in projection). However, it is more distant than M87 by 1.2 ± 0.6 Mpc based on the measurement of the planetary nebula luminosity function (Jacoby et al. 1990). The Virgo system itself is considered to have an enormously large depth in the line of sight ($15 \sim 20$ Mpc, Fukugita, Okamura, & Yasuda 1993, Yasuda, Fukugita, & Okamura 1997). The relative velocity between the single galaxies, M87 and M86, is estimated to be ~ 1500 km s $^{-1}$ (Binggeli, Sandage, & Tammann 1985). When the heliocentric velocities are averaged over the M87 and M86 subclusters, within $60'$ from each galaxy, the 2 subclusters indicate ~ 1100 km s $^{-1}$ for M87 and ~ 600 km s $^{-1}$ for M86, respectively. Because the subcluster average inevitably includes some overlapping galaxies in the boundary, we should take 500 km s $^{-1}$ as the minimum velocity for the approaching speed of M86 to M87. We will, therefore, use a velocity of 1500 km s $^{-1}$ for the later estimation.

If these 2 subclusters are still separated in the line of sight, we expect the velocity distribution in the direction of the M86 subcluster to show 2 peaks because the sample should contain foreground M87 galaxies. However, the observed distribution shows a single broad profile with a flat top. This suggests that some part of the M86 subcluster has already merged into the M87 subcluster. In this case, the resultant velocity dispersion becomes very large because the subcluster bulk motion is added to the original dispersion. This seems to be the case around M86, which shows a large velocity dispersion compared with other Virgo fields (left panel of figure 11). Also, the ROSAT observation of M86 shows a sharp drop in X-ray the surface brightness on the M87 side (Rangarajan et al. 1995). This apparent compression of the M86 interstellar matter may be caused by the interaction with the M87 subcluster. These features strongly suggest that M87 and M86 subclusters are already

interacting with each other.

The ICM temperature is expected to rise due to the subcluster merger. For simplicity, we assume that the total kinetic energy of the subcluster is fully converted to the thermal energy. Using the relative colliding velocity v_{col} , the resultant temperature increase is given by,

$$k\Delta T = \frac{1}{3}\mu m_{\text{p}}v_{\text{col}}^2 \simeq 4.7 \text{ keV} \left(\frac{v_{\text{col}}}{1500\text{km s}^{-1}} \right)^2$$

where μ is the mean molecular weight (0.6) in amu, and m_{p} is the proton mass, respectively. The ASCA results do not indicate such a high temperature around M86. Even if we may assume that the high temperature component, once created, is screened out by the large depth of the Virgo ICM, we can not explain the absence of excess X-ray brightness especially in the region between M87 and M86. Therefore it seems more reasonable to suppose that the M86 subcluster is in the very early stage of a merger and that the heating of the ICM is just about to occur.

Contrary to the large velocity dispersion, the ICM temperature in the M86 region is similar to or lower than the other regions at the same distance from M87. This pushes β_{spec} unusually high above 2.0 (right panel of figure 11). In the early stage of a subcluster merger the velocity distribution naturally creates a broad profile due to the bulk motion, even before the actual collision takes place. In fact, N-body and hydrodynamic numerical simulations indicate that the velocity dispersion increases slowly at first before the rise of the ICM temperature (Takizawa 1999). Therefore, the observed high β_{spec} value around M86 is likely to indicate the beginning of the merger. Similar high β_{spec} values above 2.0 are seen in other northwest regions, suggesting that the infall of the gas into the gravitational potential has not fully generated the thermal energy in this region. The lower average temperature and the large fluctuation suggest that the dynamical process is going on in this part of the Virgo cluster, most clearly represented by the M86 subcluster.

Another large subcluster, M49 system, has a similar geometrical configuration to the M86 one. Its location is about 1.2 Mpc south of M87 and further away by 0.6 ± 0.7 Mpc. From the ROSAT observation, the X-ray contours of M49 are elongated in the northeast-southwest direction, and a bow shock-like structure is evident in $\sim 4'$ north of the M49 center. The relative velocity at this position, estimated from a pressure balance between the ISM of M49 and the ICM of the Virgo cluster, is $\sim 1300 \text{ km s}^{-1}$ which is a reasonable value for the infall velocity of M49 into the cluster center (Irwin & Sarazin 1996). ASCA observations have revealed a remarkable hot region with $kT \sim 4 \text{ keV}$ in the middle of M87 and M49 (Kikuchi et al. 2000), refining the previous Ginga results (Koyama, Takano, & Tawara 1991). In the case of M49 subcluster, the shock heating seems to have already started. However, it is puzzling that we do not find a high temperature component in the more closer region to M49, where the shock feature is suggested. One possibility is that our observing angle is rather close to the face-on configuration to the shock front. In this case, the temperature averaged over the line-of-sight does not show a clear edge, which is also demonstrated by numerical simulations (Takizawa 2000). Therefore, it is likely that the M49 subcluster is in a somewhat advanced stage of a merger process with M87, compared with the M86 case.

4.3. Non-thermal Emission

Based on the best statistical data so far available for the Virgo cluster, we have searched for the non-thermal emission in the combined GIS spectrum and detected no significant hard X-ray component with an upper limit of $L_X^{\text{hard}} \sim 9 \times 10^{41}$ ergs s⁻¹ in the 2 – 10 keV band. This is comparable to the contribution from contaminating sources or from discrete X-ray sources in the member galaxies within a factor of 1.5. The expected amplitude of the CXB fluctuation is $\sim 2 \times 10^{41}$ ergs s⁻¹ for the average of the integrated fields. The reported luminosities of the non-thermal emission from Coma cluster, A2199, and A2256 are $0.3 - 1.1 \times 10^{44}$ ergs s⁻¹ in the energy band 2 – 10 keV. Therefore, the upper limit for the Virgo cluster is lower by 1 – 2 orders of magnitude, suggesting that the non-thermal activity over the cluster scale is almost absent in this cluster. The upper limit on the luminosity is comparable to the hard X-ray emission from the galaxy group HCG62, which clearly shows an excess hard X-ray component in the ASCA data ($\sim 8 \times 10^{41}$ ergs s⁻¹; Fukazawa et al. 2000). Considering that all the hot regions recognized in the Virgo cluster indicate the spatial size of galaxy groups, it may be that the non-thermal activities occurring in this cluster are confined to regions of the size of groups. In this sense, the Virgo cluster is a young unevolved system, and more large-scale gas heatings would probably take place in future.

5. Conclusion

The Virgo cluster is the nearest system and enables us to study of the temperature distribution with sufficient spatial resolution by ASCA. We have obtained the full temperature map of this cluster for the first time, and found significant variation of the temperature with a spatial scale of about 300 kpc. This feature is probably an evidence that heating of the ICM proceeds with infall or mergers of gas clouds which have the size of galaxy groups, as expected from the current scenario of the structure formation. Comparison of the thermal energy of the ICM and the velocity dispersion of member galaxies have been carried out for the whole Virgo system. We have reached a picture that the M86 and M49 subclusters are in a different stage of subcluster mergers, with M86 just in the pre-heating phase and M49 already entered a shock heating phase. We have not detected extended non-thermal emission from the Virgo cluster. Even the upper limit is much lower than those of other rich clusters (Coma cluster, A2199, and A2256), but is comparable to that of the galaxy group HCG62. We expect that future X-ray observations would detect more evidences of such a local heating of the ICM in other clusters and give us a comprehensive view of the actual process of the cluster evolution.

We would like to express our thanks to the ASCA team and the ASCA_ANL, SimASCA, and SimARF software development team for constructing excellent frameworks for the analysis. We also thank Dr. Y. Ikebe, T. Reiprich, M. Takizawa and H. Inoue for valuable advice on the analysis method and stimulating discussions. Useful comments from the referee Dr. J. Irwin are gratefully

acknowledged. R. S. acknowledges support from the Japan Society for the Promotion of Science (JSPS) for Young Scientists. This work was supported in part by a Grant-in-Aid for Scientific Research No. 12304009 from JSPS.

REFERENCES

- Abell, G. O., Corwin, H. G., & Jr., Olowin, R. P. 1989, ApJS, 70, 1
- Anders, E., & Grevesse, N., 1989, Geochim. Cosmochim. Acta, 53, 197
- Awaki, H., et al. 1994, PASJ, 46 L65
- Bautz, L. P. & Morgan, W. W. 1970, ApJ, 162, L149
- Böhringer, H., et al. 1994, Nature, 368, 828
- Binggeli, B., Sandage, A., & Tammann, G. A., 1985, ApJ, 90, 1681
- Binggeli, B., Tammann, G. A., & Sandage, A., 1987, ApJ, 94, 251
- Binggeli, B. & Cameron, L. M., 1993, A&AS, 98, 297
- Burke, B. E., et al., 1991, IEEE Trans. ED-38, 1069
- Churazov, E., et al. 1999, ApJ, 520, 105
- Davis, D. S., & White, R. E., 1998, ApJ, 492, 57
- Donnelly, R. H., et al. 1998, ApJ, 500, 138
- Egger, R. J., & Aschenbach, B. 1995, A&A, 294, L25
- Fabricant, D., & Gorenstein, P., 1983, ApJ, 267, 535
- Federspiel, M., Tammann, G. A., & Sandage, A., 1998, ApJ, 495, 115
- Frenk, C. S., et al. 1996, ApJ, 460, 484
- Fukazawa, Y., et al. 2000, ApJ, *in press*
- Fukugita, M., Okamura, S., & Yasuda, N., 1993, ApJ, 412, L13
- Fusco-Femiano, R., et al. 1999, ApJ, 513, L21
- Fusco-Femiano, R., et al. 2000, ApJ, 534, L7
- Henrikson, M. J., & Markevitch, M. L., 1996, ApJ, 466, L79
- Henry, J. P., & Briel, U. G., 1996, ApJ, 472, 137
- Honda, H., et al. 1996, ApJ, 473, L71
- Ishisaki, Y., 1996, ISAS Research Note, Vol. 613
- Irwin, J. A. & Sarazin, C. L., 1996, ApJ, 471, 683
- Jacoby, G. H., et al. 1990, ApJ, 356, 332
- Kaastra, J. S., et al. 1999, ApJ, 519, L119
- Kikuchi, K., et al. 2000, ApJ, 531, L95
- Koyama, K., Takano, S., & Tawara, Y. 1991, Nature, 350, 135
- Makishima, K., et al. 1989, PASJ, 41, 697

- Makishima, K., et al. 1996, PASJ, 48, 171
- Markevitch, M. R., et al. 1998, ApJ, 503, 77
- Markevitch, M. R., et al. 1999, ApJ, 521, 526
- Matsumoto, H., et al. 1996, PASJ, 48, 201
- Matsumoto, H., et al. 1997, ApJ, 482, 133
- Matsumoto, H., et al. 2000, Adv. Space Res., 25, 599
- Matsushita, K., et al. 1994, ApJ, 436, L41
- Matsushita, K., et al. 2000, PASJ, 52, 685
- Mewe, R., Lemen, J.R., & van den Oord, G.H.J. 1986, A&AS, 65, 511
- Molendi, S., et al. 1999, ApJ, 525, 73
- Neilsen, E. H., Jr, & Tsvetanov, Z. I., 2000, ApJ, 536, 255
- Ohashi, T., et al. 1996, PASJ, 48, 157
- Rangarajan, F. V. N., et al. 1995, MNRAS, 277, 1047
- Rood, H. J. & Sastry, G. N. 1971, PASP, 83, 313
- Rosati, P., et al. 1998, ApJ, 492, L21
- Sarazin, C. L., 1988, "X-ray Emission from Cluster of Galaxies", Cambridge University Press
- Schindler, S., Binggeli, B., & Böhringer, H., 1999, A&A, 343, 420
- Schwobe, A. D., et al. 2000, Astron. Nachr., 321, 1
- Serlemitsos, P. J., et al., 1995, PASJ, 47, 105
- Shibata, R., et al., 1999, ApJ, 524, 603
- Shibata, R., et al., 2000, in preparation (next paper)
- Snowden, S L., et al. 1995, ApJ, 454, 643
- Stark, A A., et al., 1992, ApJS, 79, 77
- Takano, S. 1990, Ph.D. thesis, Univ. of Kyoto
- Takizawa, M., 1999, ApJ, 520, 514
- Takizawa, M., 2000, ApJ, 532, 183
- Tanaka, Y., Inoue, H. & Holt, S. S., 1994, PASJ, 46, L37
- Tsusaka, Y., et al., 1995, Appl. Opt., 34, 4848
- Ueda, Y., et al. 1999, ApJ, 518, 656
- Voges, W., et al., 1999, A&A, 349, 389
- Watanabe, M., et al. 1999, ApJ, 827, 80

Yasuda, N., Fukugita, M., & Okamura, S., 1997, ApJS, 108, 417

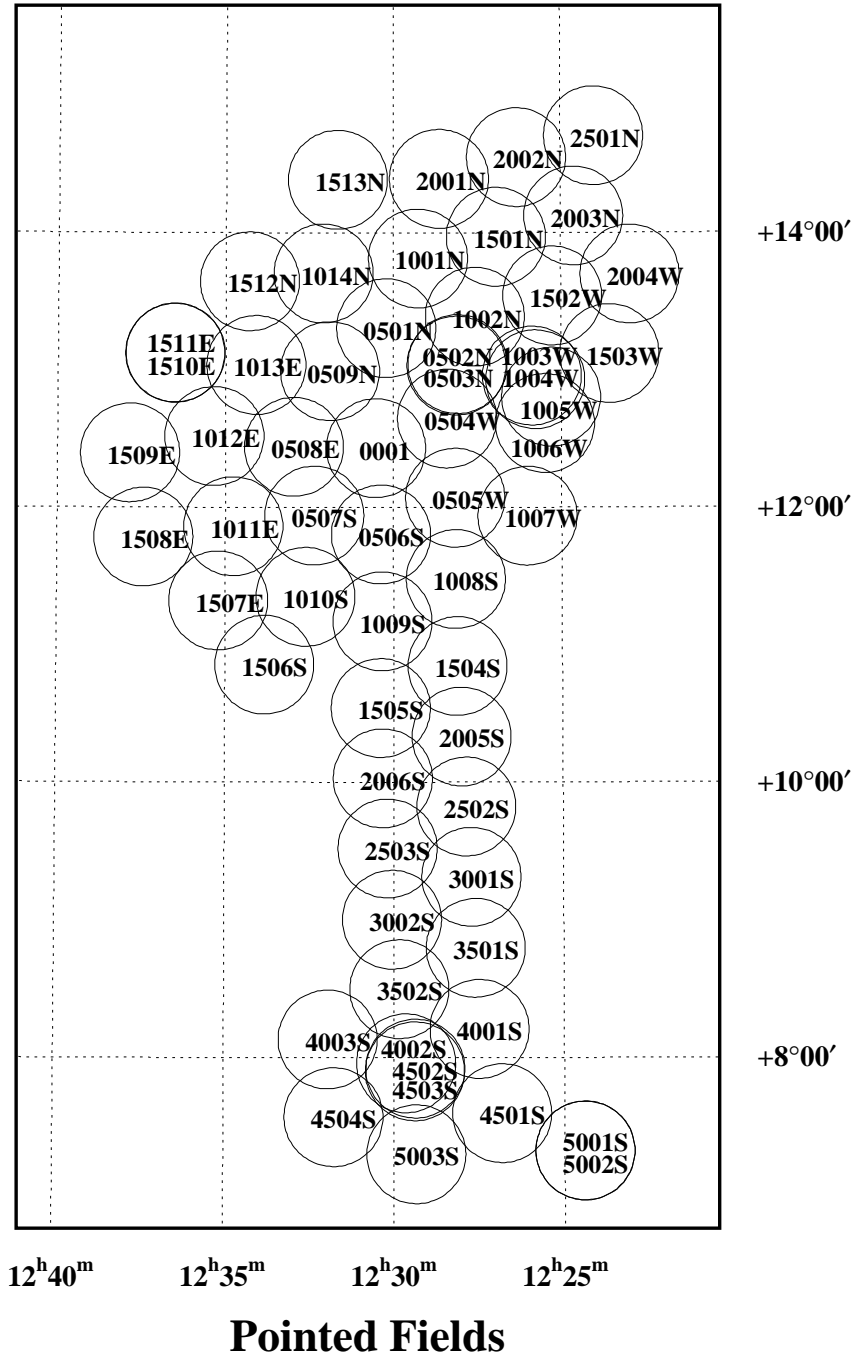


Fig. 1.— Pointed fields observed with ASCA. The observational parameters are listed in table 1. Radius of each circle is 22' corresponding to the GIS field of view.

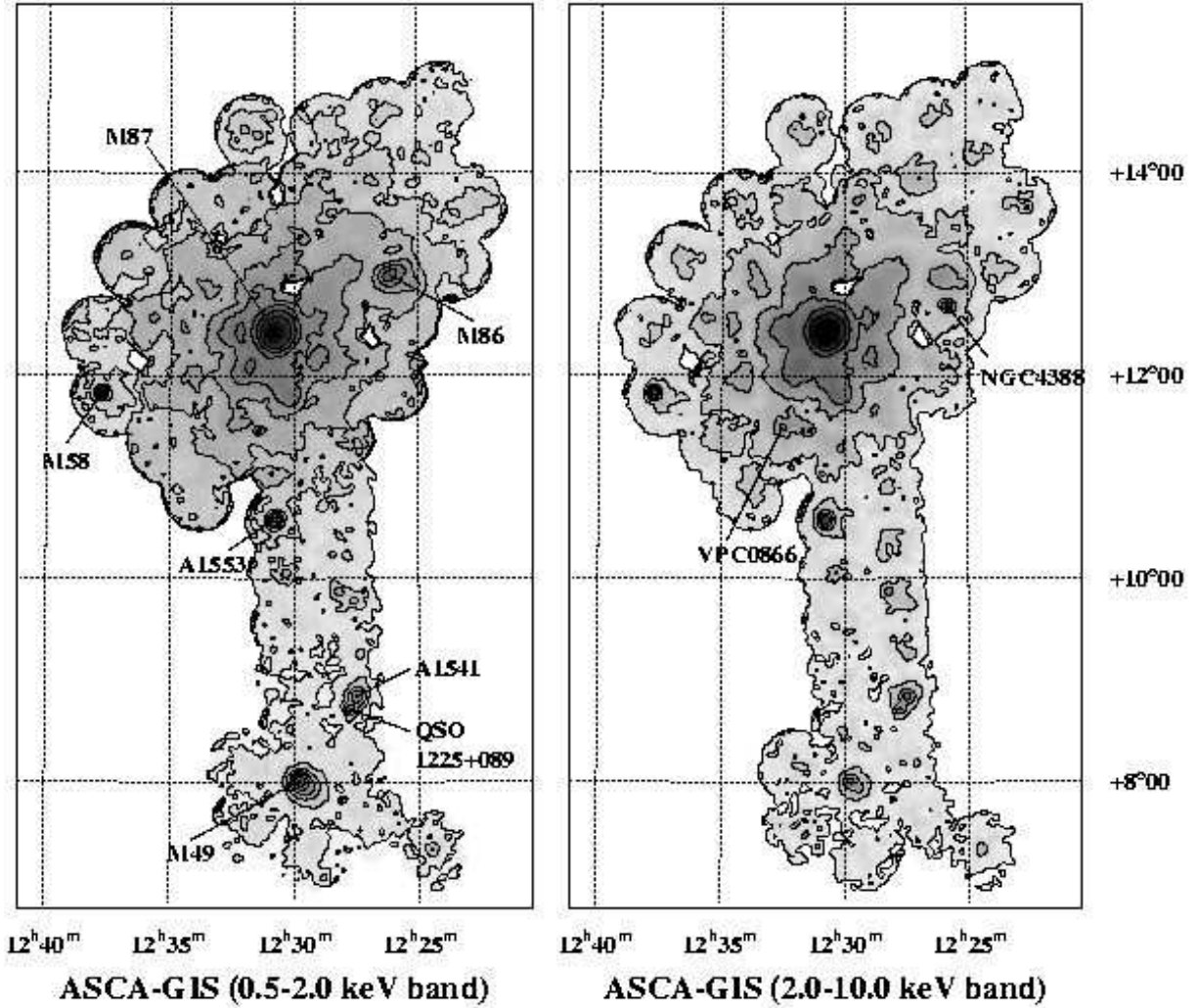


Fig. 2.— (*left*): A 0.5 – 2.0 keV band image of the Virgo cluster. (*right*): A 2.0 – 10.0 keV band image of the Virgo cluster. Each image is smoothed by a Gaussian function with $\sigma = 1.5'$, with background and vignetting effect not corrected for. Contour levels are logarithmic scale with a step factor of 1.78.

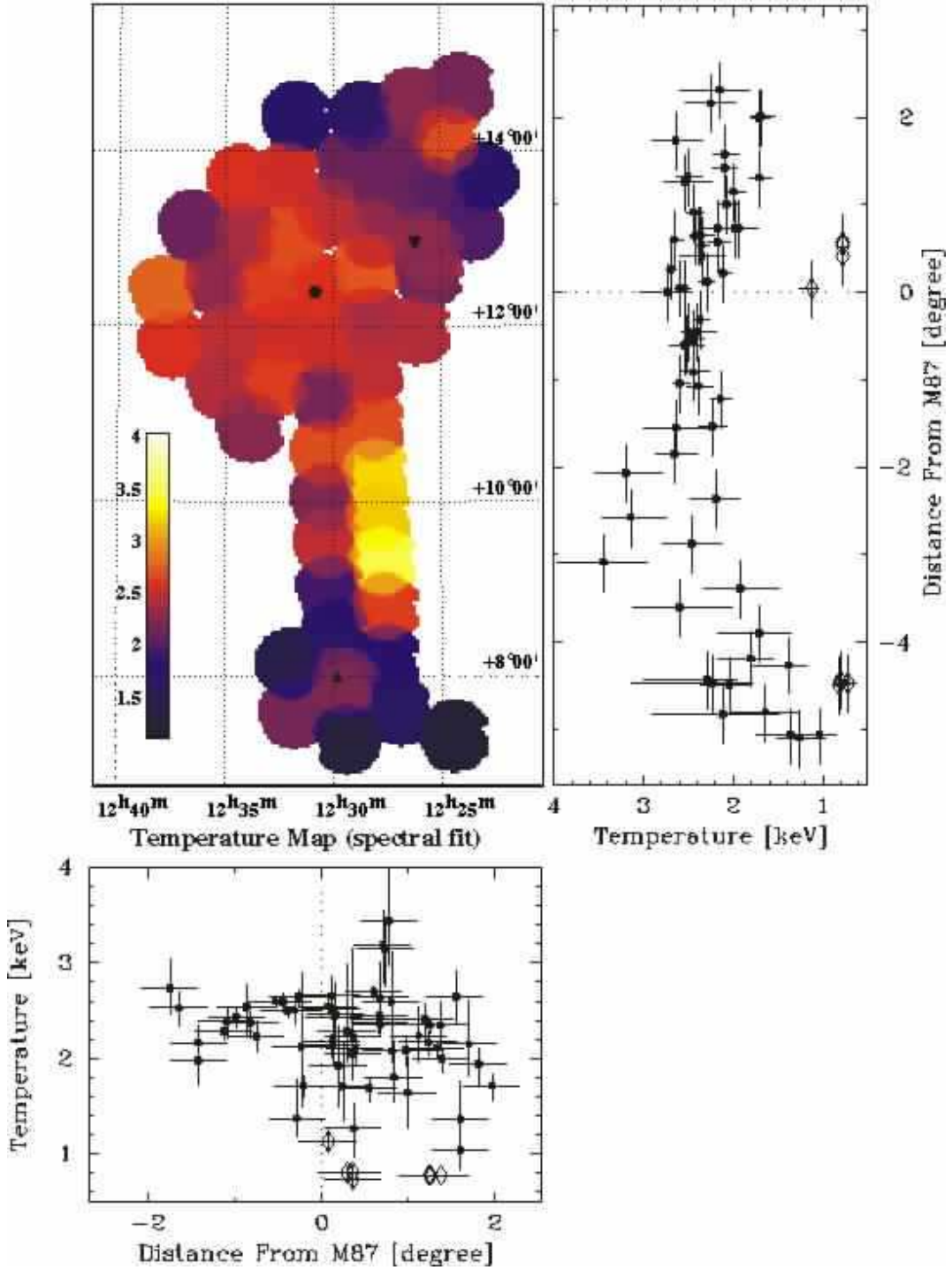


Fig. 3.— ICM temperature map of the Virgo cluster, estimated by the spectral fits for each GIS field of view. (*top-left*): Two dimensional temperature map. The positions of three galaxies are marked: M87 (circle), M86 (inverse triangle), M49 (triangle). (*top-right*): Projected temperature distribution in the north to south direction. (*bottom*): Projection in the east to west direction. Diamonds indicate the cool component (i.e., ISM) in M87, M86 and M49.

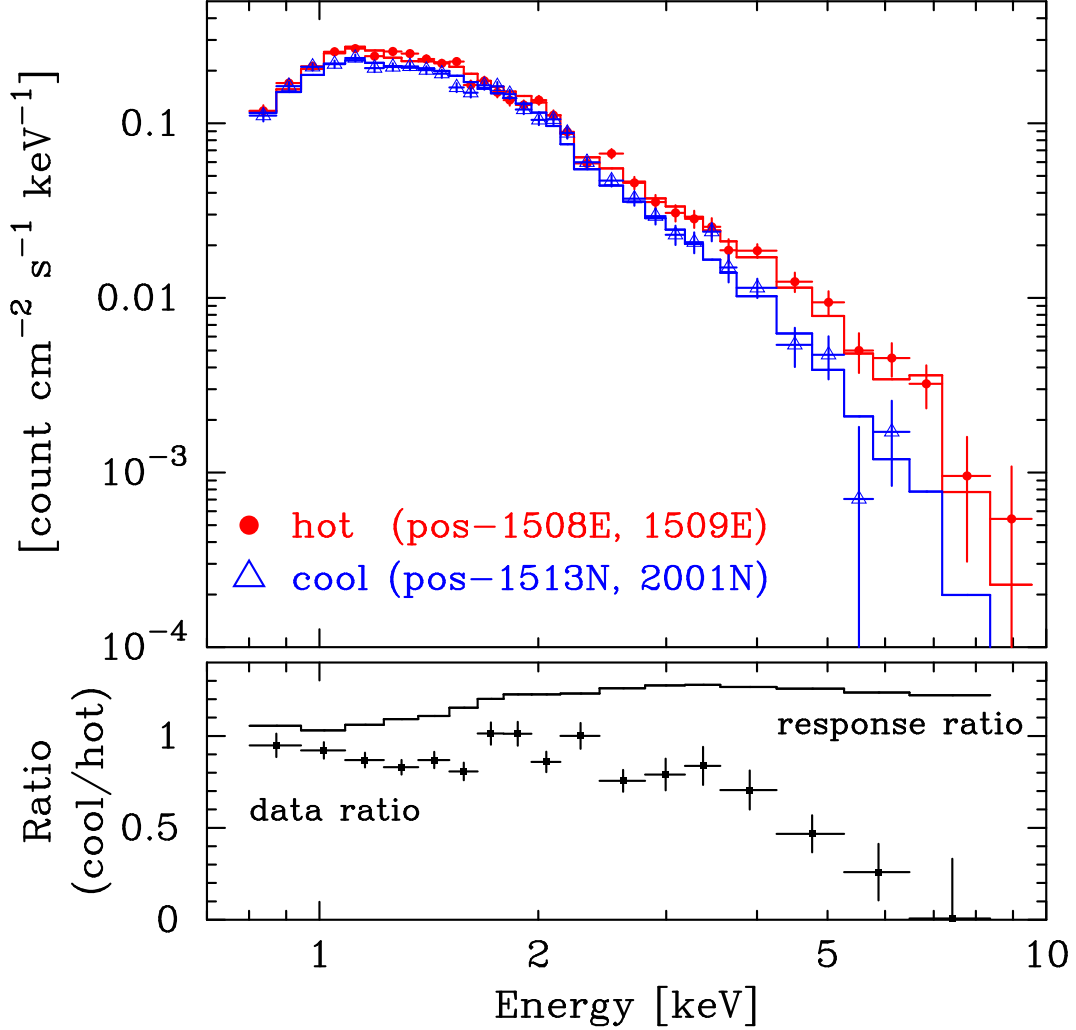


Fig. 4.— (*top*): Observed GIS spectra of the hot (pos-1508E and 1509E, filled circle) and cool (pos-1513N and 2001N, open triangle) regions. The best-fit spectra of the MEKAL model are shown as solid lines. Best-fit temperatures are $2.65^{+0.15}_{-0.16}$ keV and $1.71^{+0.11}_{-0.09}$ keV for the hot and cool regions, respectively. (*bottom*): Ratios of the observed data and the XRT response functions (i.e., effective areas of XRT) for spectral analysis.

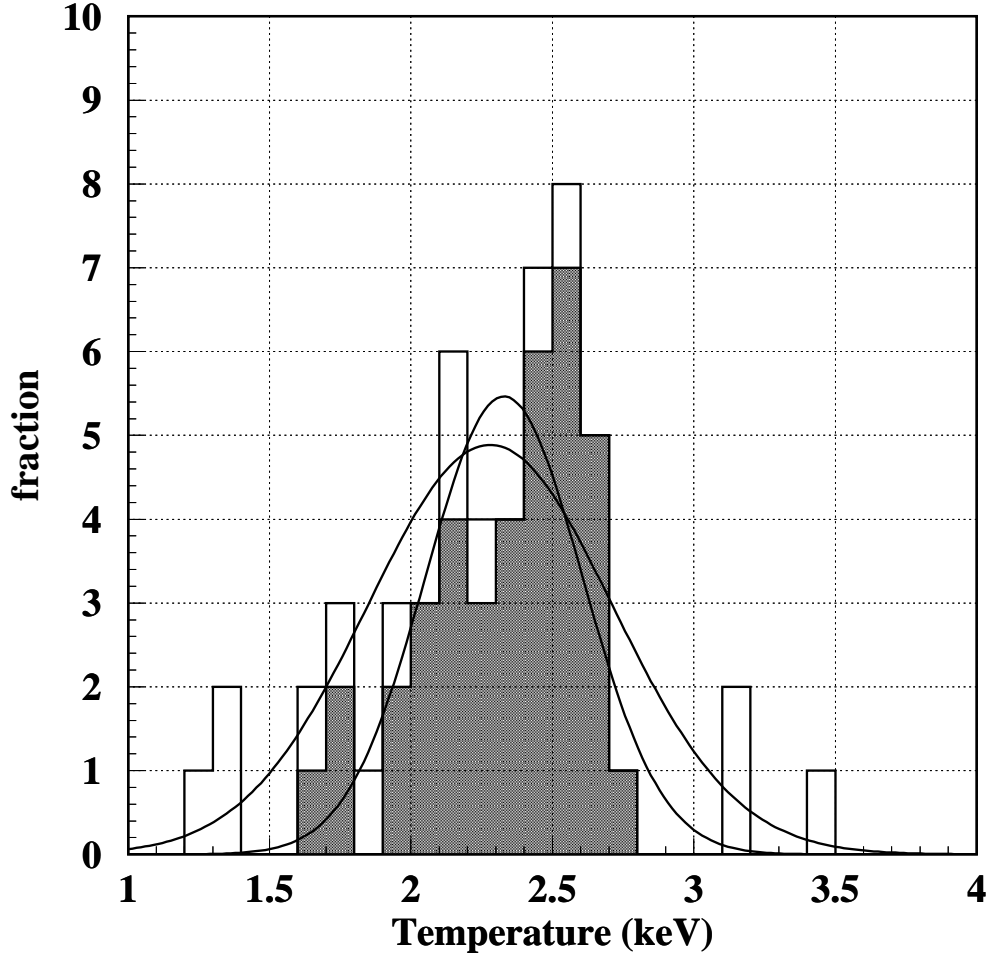


Fig. 5.— Frequency distribution of the ICM temperatures based on the spectral fits for the GIS FOV unit. Shaded and unshaded portions indicate the data within 2.5° centered on M87 and the all data in the Virgo field, respectively. We fitted these distributions with a Gaussian model. Best-fit parameters are obtained to be an average temperature of $\bar{T} = 2.33$ keV with $\sigma_{\bar{T}} = 0.28$ keV within 2.5° from M87 and $\bar{T} = 2.28$ keV with $\sigma_{\bar{T}} = 0.43$ keV for all regions.

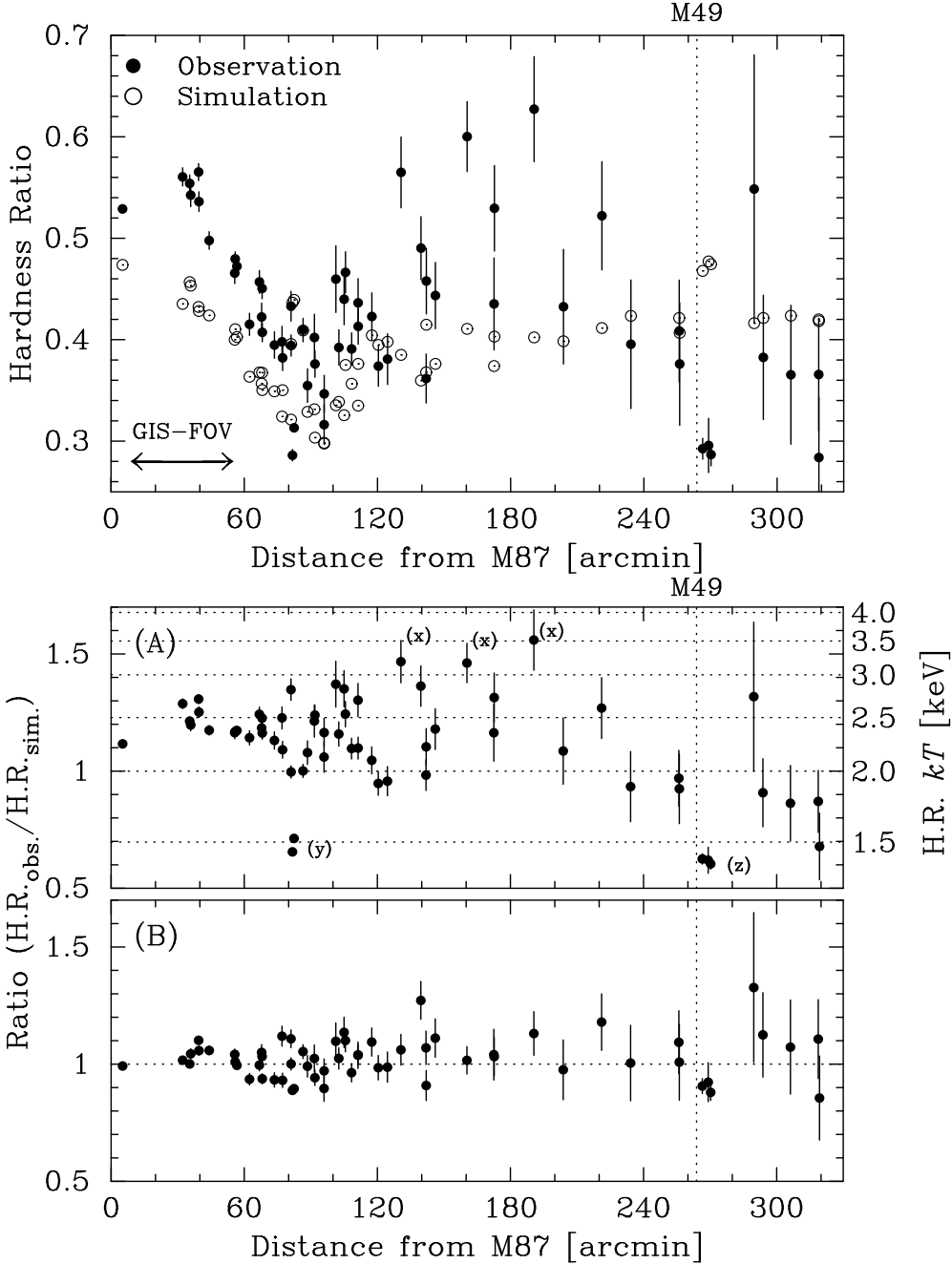


Fig. 6.— Hardness ratio from the counting rates between energy bands 2.0 – 7.0 keV and 0.7 – 2.0 keV for each pointed field ($r \sim 22'$). (*top*): Hardness ratios from the raw counting rates (filled circles, $H.R._{obs.}$) and from the ray-tracing simulation (open circles, $H.R._{sim.}$), in which the MEKAL model with an uniform temperature of 2.0 keV and a metal abundance of 0.3 solar are assumed. (*middle*): Corrected hardness ratio ($= H.R._{obs.}/H.R._{sim.}$) which take account of the difference in the response based on the simulated isothermal profile. Notations of (x), (y), and (z) indicate the high temperature region reported by Kikuchi (2000), the regions which include M86 and M49, respectively. (*bottom*): Same as a middle panel, but showing the corrected hardness ratio from the ray-tracing simulation, in which the temperature distribution of the middle panel is assumed. In all panels, errors indicate 1σ statistical limits.

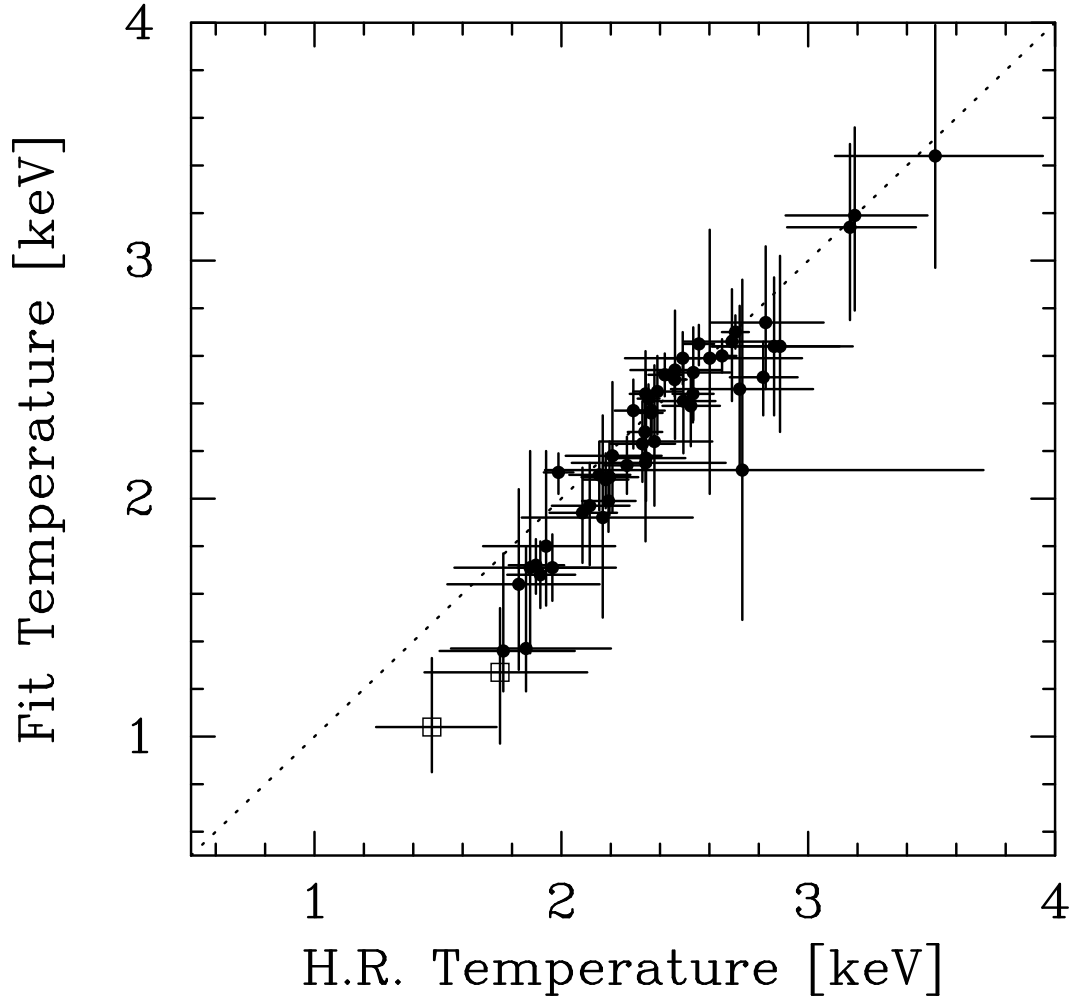


Fig. 7.— Correlation between the temperatures derived from the hardness ratio (H.R.) and from the spectral fit, except for some regions which require two temperature components. Dot line indicates the consistent temperature. Because two regions (pos-5002S and 5003S, open square) indicate much lower metal abundance (< 0.1 solar) and temperature (< 1.3 keV) compared with the model spectrum for the simulation, both temperatures are inconsistent. If we fit this correlation with a linear function, a slope is obtained to be 0.99 ± 0.01 with a χ^2_ν value of 0.72 (d.o.f. = 51).

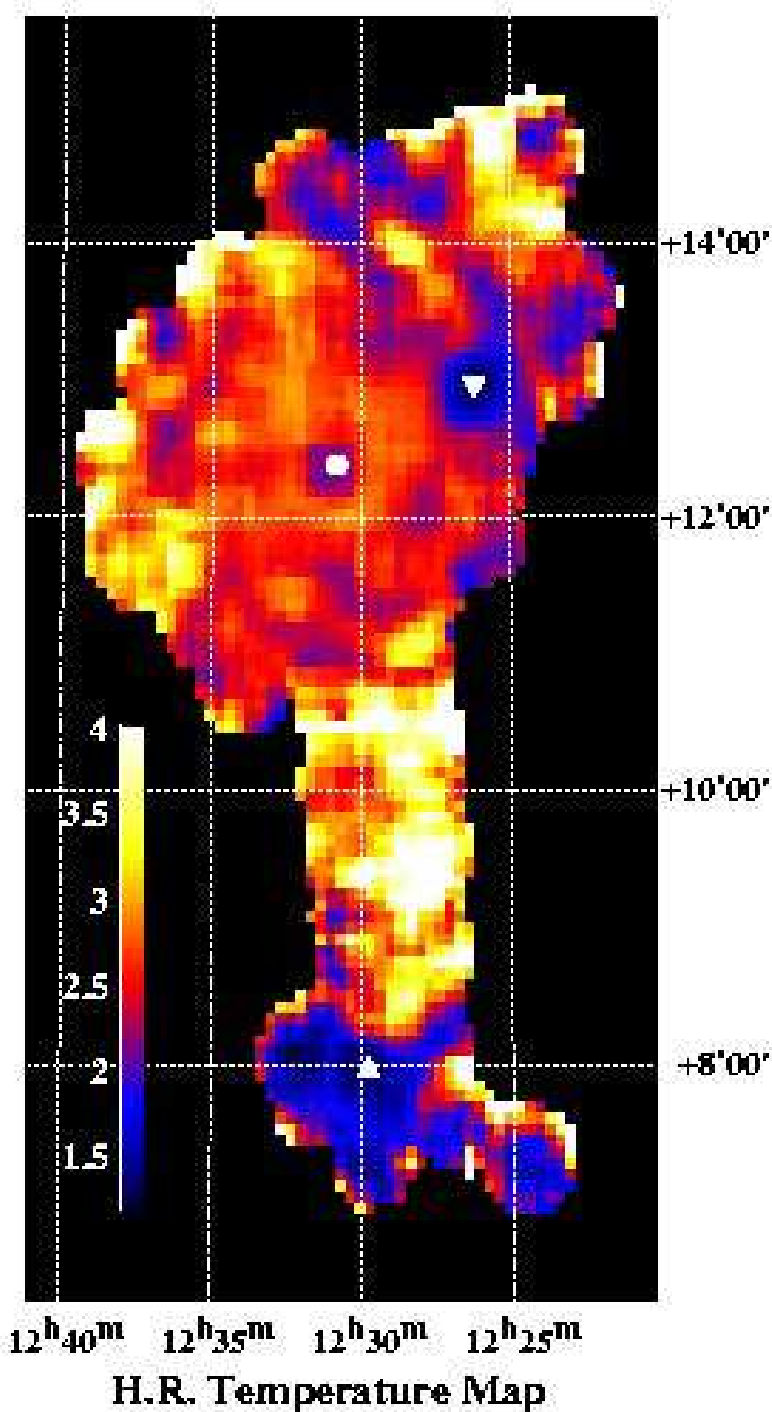


Fig. 8.— Temperature map of the Virgo cluster, based on the temperature estimation from hardness ratio. The difference of the response for each pointed field and the vignetting effect are taken into account. Each pixel size is $5' \times 5'$ square, and H.R. temperature is calculated from the average photon number ratio of the surrounding $20' \times 20'$ square in order to improve photon statistics. The source mask mentioned in section 2.2 is applied. Note that the average temperatures between the ICM and ISM are shown at the position of M87 (circle), M86 (inverse triangle) and M49 (triangle).

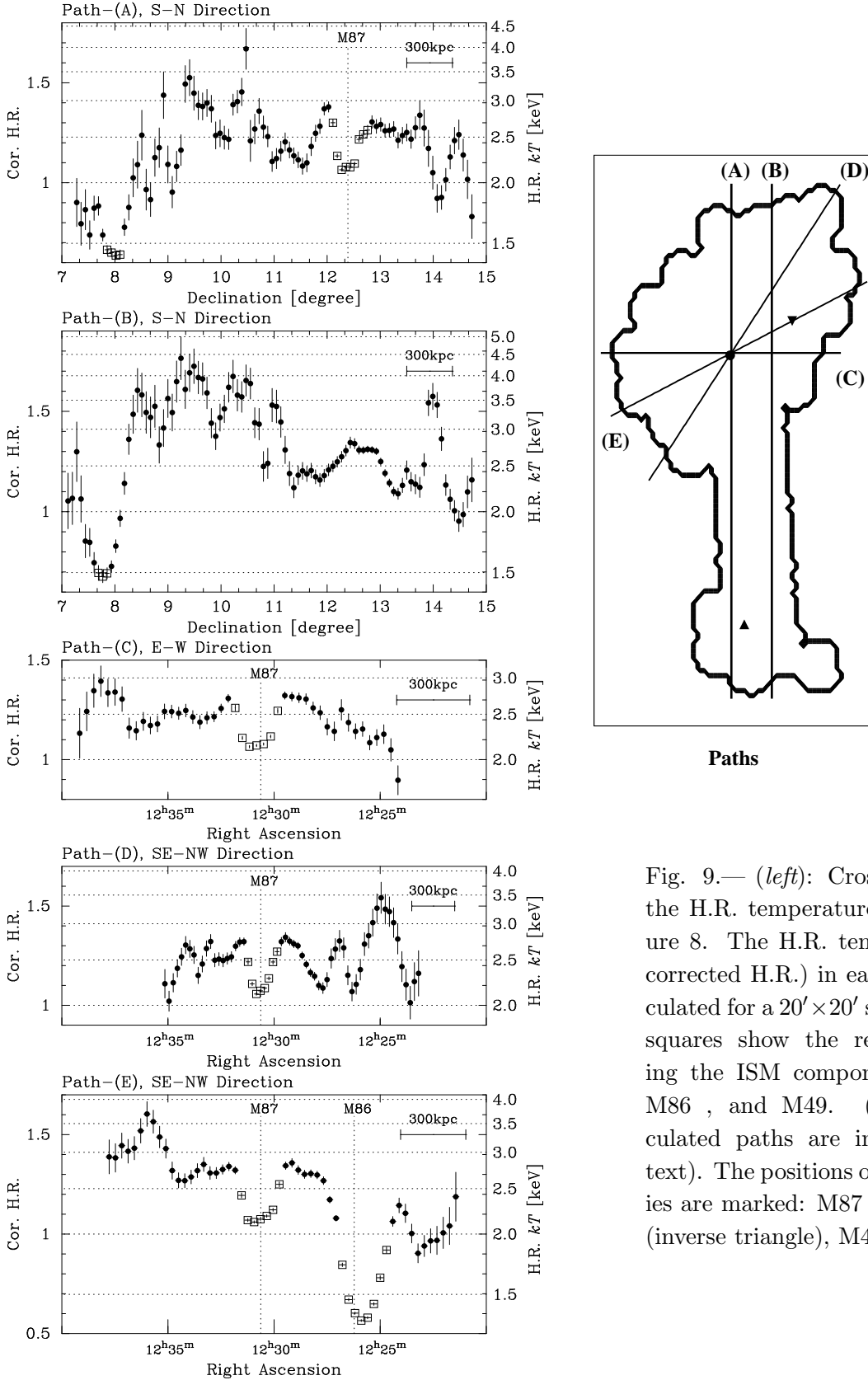


Fig. 9.— (left): Cross sections of the H.R. temperature map in figure 8. The H.R. temperature (= corrected H.R.) in each bin is calculated for a $20' \times 20'$ square. Open squares show the region including the ISM component of M87, M86, and M49. (right): Calculated paths are indicated (see text). The positions of three galaxies are marked: M87 (circle), M86 (inverse triangle), M49 (triangle).

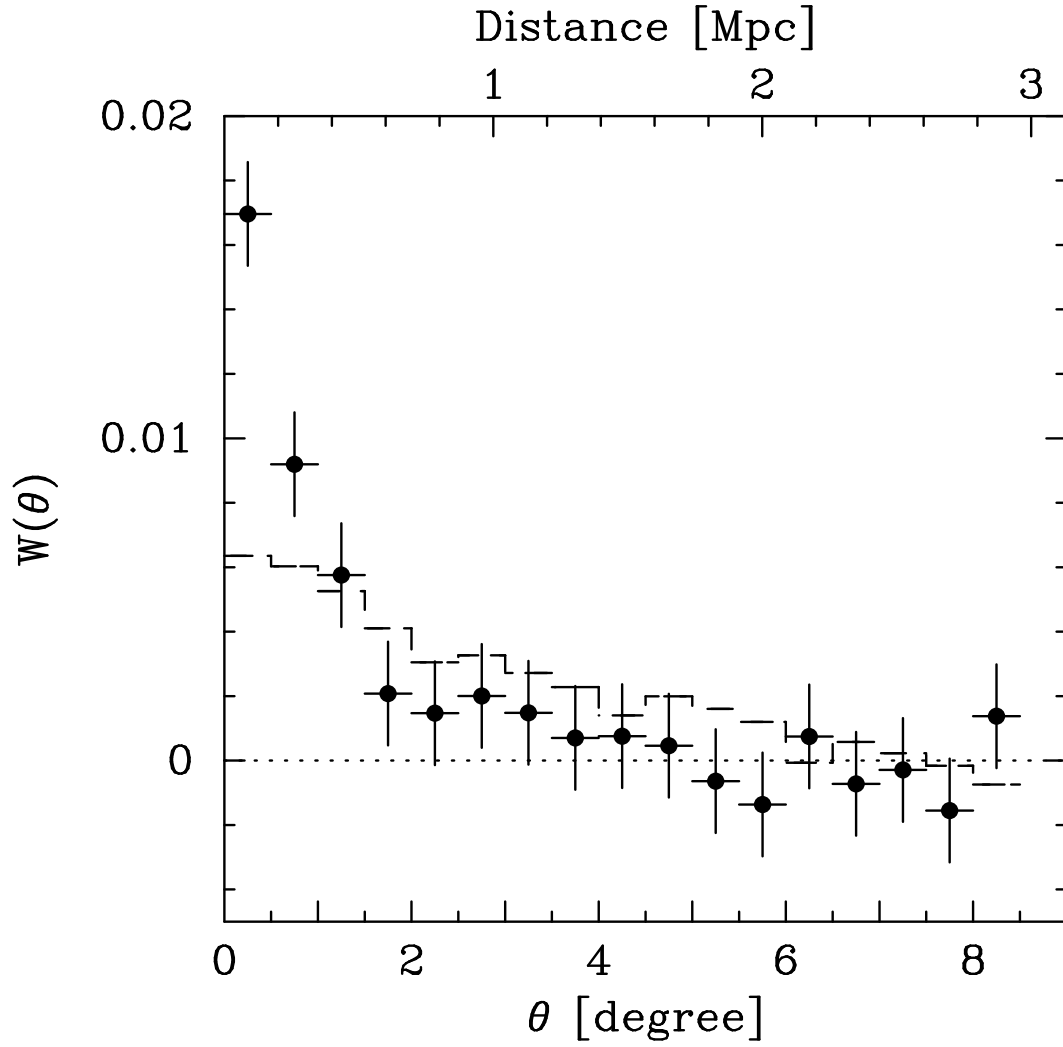


Fig. 10.— Auto-correlation function (ACF) for the two dimensional C.H.R. based on the observed data (filled circle) and the model data assuming the large-scale temperature gradient centered on M87 (broken line).

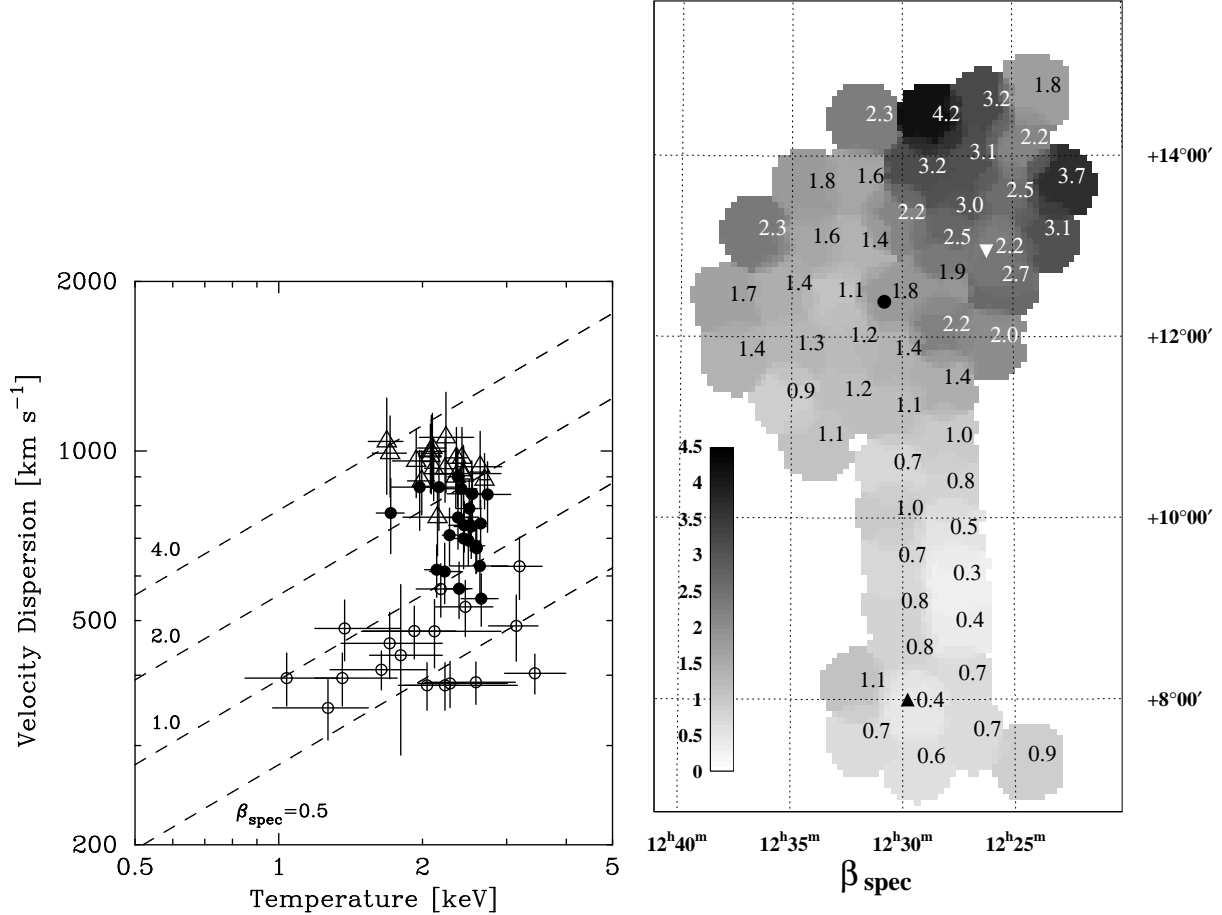


Fig. 11.— (*left*): Correlation between the velocity dispersions (σ^2) and the ICM temperatures (kT). The velocity dispersions are calculated from mean values within a radius of 1.5° centered on the GIS-FOV. The symbols indicate different regions. Triangles are for the northwest of M87 (around M86), filled circles are within 2.5° from M87 except for the northwest region, and open circles are the remaining regions, respectively. Broken lines indicate β_{spec} ($= \mu m_p \sigma^2 / kT$) values = 0.5, 1.0, 2.0 and 4.0, respectively. (*right*): β_{spec} map of the Virgo cluster. The positions of three bright galaxies are marked: M87 (circle), M86 (inverse triangle), M49 (triangle).

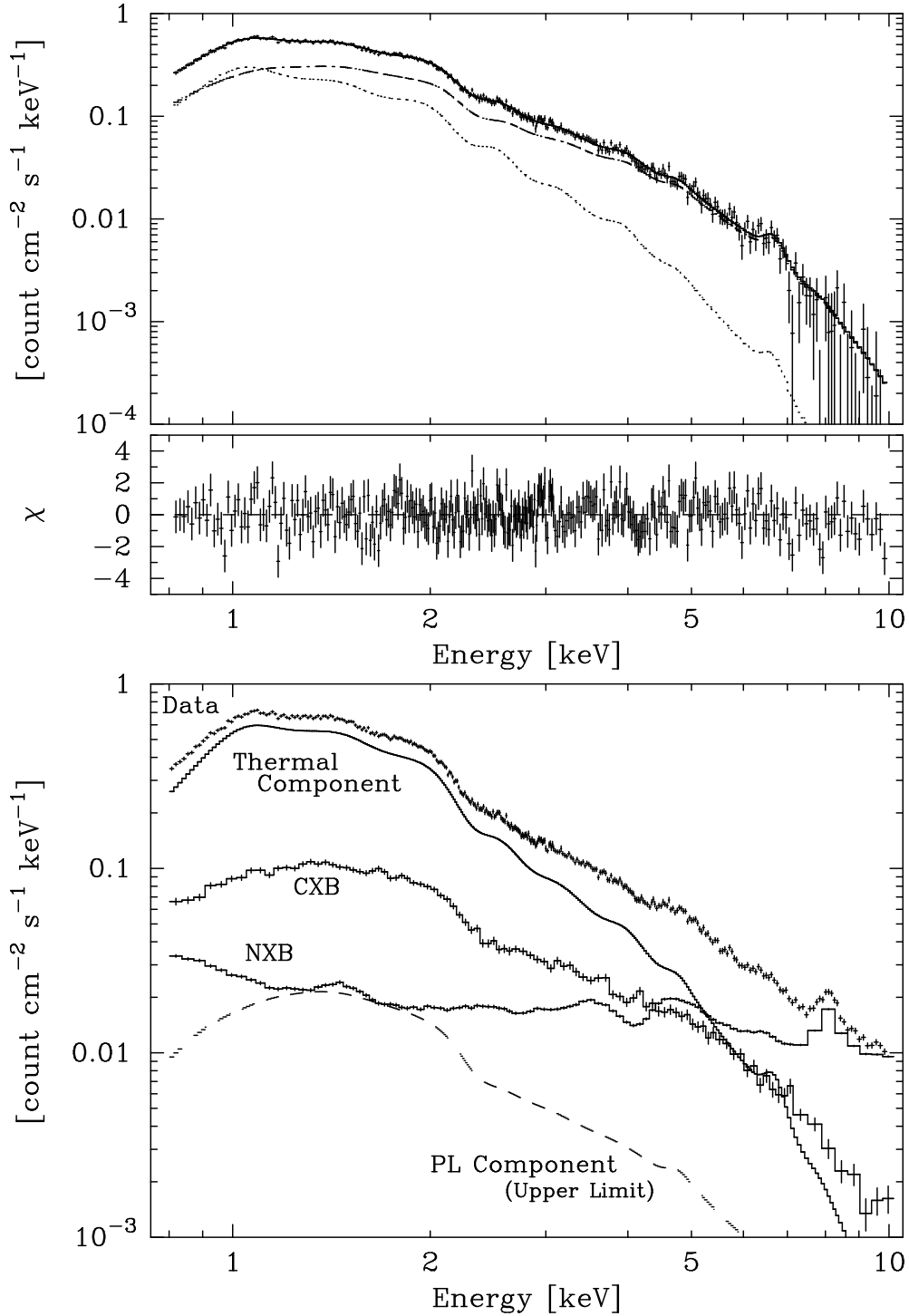


Fig. 12.— (*top*): The Average Virgo spectrum within $r = 0.4^\circ - 2.5^\circ$ centered on M87 (cross mark), the best-fit two temperature MEKAL model (line) which consists of hot and cool components (broken and dot lines) , and the residual between the data and model. (*bottom*): Each component in the above spectrum (observed data, CXB, and NXB spectra) together with the model spectrum (thermal component and upper limit of the PL component).

Table 1:: Log of ASCA observations and result of spectral fits

Pointing [†] Name	R.A., Dec. [deg.](J2000)		Dist. [‡] [arcmin.]	Date [§] [UT]	Exp.* [sec]	Rate [¶] [c/s]	Temperature [£] [keV]	χ^2 (d.o.f)
0001 ^(a)	187.63	12.43	5	93/06/07	12017	8.278	2.54 ^{+0.12} _{-0.06} , 1.12 ^{+0.16} _{-0.07}	916.2 (537)
0501N	187.55	13.31	56	97/06/14	9461	1.015	2.44 ^{+0.10} _{-0.11}	105.1 (95)
0502N	187.03	13.03	56	95/12/24	20784	1.079	2.42 ^{+0.06} _{-0.07}	147.0 (95)
0503N	187.02	13.04	57	96/01/05	17820	1.092	2.36 ^{+0.07} _{-0.13}	176.0 (95)
0504W	187.10	12.65	39	93/06/08	11392	1.342	2.70 ^{+0.07} _{-0.07}	161.7 (95)
0505W	187.04	12.07	44	99/06/21	10159	1.240	2.37 ^{+0.08} _{-0.10}	142.9 (95)
0506S	187.59	11.80	36	98/06/11	4811	1.752	2.52 ^{+0.09} _{-0.09}	105.4 (95)
0507S	188.09	11.94	35	99/06/23	9227	1.584	2.50 ^{+0.06} _{-0.07}	124.3 (95)
0508E	188.24	12.44	32	99/06/23	8596	1.501	2.60 ^{+0.07} _{-0.07}	120.1 (95)
0509N	187.97	12.99	40	99/06/23	10486	1.136	2.65 ^{+0.08} _{-0.09}	116.2 (95)
1001N	187.32	13.81	89	96/12/27	7902	0.600	2.10 ^{+0.14} _{-0.15}	82.3 (64)
1002N	186.89	13.39	77	96/12/27	8308	0.786	2.08 ^{+0.11} _{-0.12}	74.0 (64)
1003W ^(b)	186.47	12.96	82	93/07/03	16920	1.019	2.17 ^{+0.14} _{-0.13} , 0.78 (fix)	128.4 (94)
1004W ^(b)	186.44	12.93	82	98/06/09	76313	1.036	2.35 ^{+0.07} _{-0.09} , 0.78 (fix)	172.4 (94)
1005W ^(b)	186.33	12.81	86	93/07/04	18314	0.858	2.35 ^{+0.26} _{-0.26} , 0.78 (fix)	79.0 (70)
1006W	186.37	12.61	81	95/06/21	20218	0.732	2.11 ^{+0.08} _{-0.09}	88.3 (62)
1007W	186.50	11.94	77	99/06/22	10434	0.576	2.41 ^{+0.19} _{-0.22}	89.1 (64)
1008S	187.04	11.48	68	98/06/11	10323	0.669	2.45 ^{+0.15} _{-0.18}	87.2 (64)
1009S	187.58	11.17	74	98/06/11	12379	0.651	2.14 ^{+0.12} _{-0.12}	78.0 (64)
1010S	188.15	11.35	68	99/06/22	12975	0.827	2.59 ^{+0.11} _{-0.11}	72.1 (64)
1011E	188.69	11.86	67	99/06/30	12530	0.762	2.44 ^{+0.11} _{-0.12}	79.5 (64)
1012E	188.83	12.52	68	95/06/26	18392	0.749	2.28 ^{+0.12} _{-0.08}	76.9 (64)
1013E	188.52	13.04	62	99/07/02	10825	0.788	2.37 ^{+0.13} _{-0.16}	64.1 (64)
1014N	188.02	13.71	81	99/06/24	15105	0.531	2.51 ^{+0.15} _{-0.16}	72.1 (64)
1501N	186.73	13.97	111	97/06/16	17547	0.473	2.09 ^{+0.15} _{-0.16}	85.6 (64)
1502W	186.31	13.54	108	96/12/26	19271	0.445	1.99 ^{+0.13} _{-0.13}	77.1 (64)
1503W	185.89	13.12	117	96/12/26	17043	0.384	1.94 ^{+0.19} _{-0.21}	85.4 (64)
1504S	187.03	10.85	101	98/06/12	10210	0.364	2.64 ^{+0.38} _{-0.36}	72.3 (64)
1505S	187.59	10.54	111	96/06/12	31134	0.522	2.66 ^{+0.22} _{-0.25}	69.1 (64)
1506S	188.46	10.85	103	99/06/26	15839	0.442	2.23 ^{+0.18} _{-0.16}	71.2 (64)
1507E	188.80	11.32	92	99/06/26	19172	0.519	2.39 ^{+0.15} _{-0.17}	88.7 (64)
1508E	189.36	11.78	106	95/06/25	22836	0.485	2.53 ^{+0.19} _{-0.20}	75.0 (64)

continued on next page

continued from previous page

Pointing [†] Name	R.A., Dec. [deg.](J2000)		Dist. [‡] [arcmin.]	Date [§] [UT]	Exp.* [sec]	Rate [¶] [c/s]	Temperature [£] [keV]	χ^2 (d.o.f)
1509E	189.46	12.40	105	99/07/01	16227	0.366	$2.74^{+0.32}_{-0.28}$	81.4 (64)
1510E	189.13	13.12	96	97/06/24	16054	0.432	$2.17^{+0.18}_{-0.18}$	75.0 (64)
1511E	189.13	13.13	96	97/07/06	14472	0.427	$1.97^{+0.18}_{-0.25}$	80.5 (64)
1512N	188.57	13.65	92	99/06/24	10455	0.432	$2.54^{+0.25}_{-0.29}$	60.8 (64)
1513N	187.92	14.39	120	97/06/22	28349	0.397	$1.72^{+0.11}_{-0.12}$	93.1 (64)
2001N	187.16	14.39	125	97/06/17	16349	0.356	$1.68^{+0.14}_{-0.14}$	73.6 (64)
2002N	186.58	14.55	146	97/06/16	16466	0.336	$2.24^{+0.32}_{-0.27}$	45.6 (64)
2003N	186.15	14.12	140	97/06/15	17252	0.351	$2.64^{+0.29}_{-0.29}$	78.3 (64)
2004W	185.73	13.70	142	96/12/25	18667	0.355	$1.71^{+0.14}_{-0.14}$	98.7 (64)
2005S	187.00	10.33	131	98/06/12	19671	0.334	$3.19^{+0.37}_{-0.40}$	82.5 (64)
2006S	187.58	10.03	142	98/06/12	14419	0.346	$2.18^{+0.31}_{-0.24}$	82.1 (64)
2501N	186.00	14.71	172	97/06/14	22875	0.281	$2.15^{+0.47}_{-0.33}$	59.8 (64)
2502S	186.96	9.82	160	98/06/13	19100	0.359	$3.14^{+0.35}_{-0.39}$	104.1 (64)
2503S	187.55	9.52	173	98/06/13	17033	0.299	$2.46^{+0.35}_{-0.33}$	62.1 (64)
3001S	186.93	9.31	191	98/06/17	18154	0.294	$3.44^{+0.55}_{-0.47}$	61.8 (64)
3002S	187.51	9.00	204	98/06/17	17335	0.264	$1.92^{+0.43}_{-0.42}$	62.0 (64)
3501S	186.90	8.80	221	98/06/18	16544	0.402	$2.59^{+0.54}_{-0.57}$	91.7 (64)
3502S	187.46	8.50	234	98/06/23	10070	0.285	$1.71^{+0.49}_{-0.36}$	57.4 (64)
4001S	186.87	8.21	256	98/06/18	14268	0.284	$1.80^{+0.40}_{-0.25}$	84.0 (64)
4002S ^(c)	187.41	7.96	266	93/07/04	17256	0.547	$2.28^{+0.73}_{-0.32}, 0.81^{+0.07}_{-0.10}$	144.9 (93)
4003S	187.98	8.13	256	98/06/20	14092	0.271	$1.37^{+0.43}_{-0.18}$	73.6 (64)
4501S	186.71	7.60	294	98/06/19	10811	0.269	$1.64^{+0.40}_{-0.36}$	82.8 (64)
4502S ^(c)	187.34	7.92	269	93/06/30	2718	0.537	$2.23^{+0.93}_{-0.45}, 0.73^{+0.14}_{-0.11}$	98.7 (93)
4503S ^(c)	187.35	7.90	270	93/06/30	16977	0.515	$2.04^{+0.34}_{-0.21}, 0.82^{+0.08}_{-0.11}$	119.0 (93)
4504S	187.94	7.57	290	98/06/19	4476	0.262	$2.12^{+0.80}_{-0.63}$	69.5 (64)
5001S	186.10	7.33	319	93/06/27	18877	0.256	$1.36^{+0.41}_{-0.17}$	70.2 (64)
5002S	186.10	7.33	319	93/06/28	11799	0.259	$1.04^{+0.29}_{-0.19}$	79.9 (64)
5003S	187.34	7.30	306	98/12/21	11764	0.259	$1.27^{+0.27}_{-0.30}$	67.9 (64)

continued on next page

continued from previous page

Pointing [†]	R.A., Dec.	Dist. [‡]	Date [§]	Exp.*	Rate [¶]	Temperature ^ℓ	χ^2 (d.o.f)
Name	[deg.](J2000)	[arcmin.]	[UT]	[sec]	[c/s]	[keV]	

†: $ddnnD$ (dd , nn , and D show the distance range between $d.d^\circ$ and $d.d^\circ + 0.5^\circ$ from M87, serial number, and azimuth direction from M87, i.e., “North, West, South and East”, respectively).

‡: Distance from the center of M87 in arcminutes. The position of M87 is (R.A, Dec)_{J2000} = (187.7058, 12.3911).

§: Start time of observation in year/month/day.

*: Total Exposure time of GIS (per sensor) after the data screening.

¶: GIS counting rate (per sensor, 0.7-10.0 keV band) including the cosmic X-ray background and non X-ray background.

ℓ: ICM temperature estimated by spectral fit with the MEKAL model (see section 3.1).

(a)(b)(c): Pointings including three bright galaxies, M87, M86 and M49, respectively. Two temperature MEKAL model for the ICM and ISM was adopted.

Table 2: Best-fit parameters of the whole Virgo spectrum

	MEKAL model	MEKAL + MEKAL model
χ^2 (d.o.f.)	395.7 (322)	351.4 (320)
kT [keV]	2.50 ^{+0.04} _{-0.05}	3.67 ^{+0.53} _{-0.52} , 1.38 ^{+0.09} _{-0.13}
Z_{Fe} [solar]	0.26 ^{+0.04} _{-0.04}	0.16 ^{+0.04} _{-0.03}
Z_{S} [solar]	0.50 ^{+0.12} _{-0.11}	0.52 ^{+0.10} _{-0.09}
Z_{Si} [solar]	0.45 ^{+0.11} _{-0.10}	0.33 ^{+0.08} _{-0.06}
$F_X^{\text{thermal}}(2\text{-}10\text{keV})$ [ergs cm ⁻² s ⁻¹ arcmin ⁻²]	$(1.05^{+0.07}_{-0.07}) \times 10^{-14}$	$(1.09^{+0.23}_{-0.14}) \times 10^{-14}$
		+ Power-Law model
χ^2 (d.o.f.)		351.4 (319)
Photon Index		1.7 (fixed)
$F_X^{\text{hard}}(2\text{-}10\text{keV})$ [ergs cm ⁻² s ⁻¹ arcmin ⁻²]		$< 9.52 \times 10^{-16}$
$L_X^{\text{hard}}(2\text{-}10\text{keV})$ [ergs s ⁻¹]		$< 2.28 \times 10^{42}$
Flux Ratio (= $F_X^{\text{hard}}/F_X^{\text{thermal}}$)		< 0.09